Monthly Notices
of the
ROYAL ASTRONOMICAL SOCIETY

MNRAS **448,** 3167–3195 (2015) doi:10.1093/mnras/stv184

The systematic search for $z \gtrsim 5$ active galactic nuclei in the *Chandra* Deep Field South

Anna K. Weigel,[1]★ Kevin Schawinski,[1] Ezequiel Treister,[2] C. Megan Urry,[3] Michael Koss[1]† and Benny Trakhtenbrot[1]‡

[1]*Institute for Astronomy, Department of Physics, ETH Zurich, Wolfgang-Pauli-Strasse 27, CH-8093 Zurich, Switzerland*
[2]*Universidad de Concepción, Departamento de Astronomía, Casilla 160-C, Concepción, Chile*
[3]*Physics Department and Yale Center for Astronomy and Astrophysics, Yale University, New Haven, CT 06511, USA*

Accepted 2015 January 26. Received 2015 January 26; in original form 2014 October 29

ABSTRACT

We investigate early black hole (BH) growth through the methodical search for $z \gtrsim 5$ active galactic nuclei (AGN) in the *Chandra* Deep Field South. We base our search on the *Chandra* 4-Ms data with flux limits of 9.1×10^{-18} (soft, 0.5–2 keV) and 5.5×10^{-17} erg s^{-1} cm^{-2} (hard, 2–8 keV). At $z \sim 5$, this corresponds to luminosities as low as $\sim 10^{42}$ ($\sim 10^{43}$) erg s^{-1} in the soft (hard) band and should allow us to detect Compton-thin AGN with $M_{\rm BH} > 10^7$ M$_\odot$ and Eddington ratios >0.1. Our field (0.03 deg^2) contains over $600z \sim 5$ Lyman Break Galaxies. Based on lower redshift relations, we would expect $\sim$20 of them to host AGN. After combining the *Chandra* data with Great Observatories Origins Deep Survey (GOODS)/Advanced Camera for Surveys (ACS), CANDELS/Wide Field Camera 3 and *Spitzer*/Infrared Array Camera data, the sample consists of 58 high-redshift candidates. We run a photometric redshift code, stack the GOODS/ACS data, apply colour criteria and the Lyman Break Technique and use the X-ray Hardness Ratio. We combine our tests and using additional data find that all sources are most likely at low redshift. We also find five X-ray sources without a counterpart in the optical or infrared which might be spurious detections. We conclude that our field does not contain any convincing $z \gtrsim 5$ AGN. Explanations for this result include a low BH occupation fraction, a low AGN fraction, short, super-Eddington growth modes, BH growth through BH–BH mergers or in optically faint galaxies. By searching for $z \gtrsim 5$ AGN, we are setting the foundation for constraining early BH growth and seed formation scenarios.

Key words: galaxies: active – galaxies: high-redshift – X-rays: galaxies.

1 INTRODUCTION

Massive black holes (BHs) with masses $>10^6$ M$_\odot$ reside in most galaxies, including our own (Genzel et al. 1996; Ghez et al. 1998, 2000, 2008; Magorrian et al. 1998; Schödel et al. 2003). Luminous quasars with $M_{\rm BH} \sim 10^9$ M$_\odot$ (Barth et al. 2003: $z = 6.4$; Willott, McLure & Jarvis 2003: $z = 6.41$; Trakhtenbrot et al. 2011: $z \sim 4.8$) have been detected at $z \sim$ 5–7 (Fan et al. 2000, 2001: $z \sim 6$; Mortlock et al. 2011: $z = 7.085$). The BHs powering these quasars must therefore build up their mass in less than one billion years. Depending on the assumed seed formation model, almost constant Eddington accretion or even super-Eddington episodes are required to match these observations (Volonteri & Rees 2005; Alexander & Natarajan 2014; Volonteri & Silk 2014). In our current understanding, BHs grew out of $\sim$100–10^5 M$_\odot$ seeds by accreting infalling matter or merging with a second BH (Rees & Volonteri 2007). Two seed formation models are currently favoured. One scenario predicts that the remnants of massive Population III (Pop III) stars constitute BH progenitors (Haiman & Loeb 2001; Madau & Rees 2001; Bromm, Coppi & Larson 2002; Alvarez, Wise & Abel 2009; Johnson et al. 2012). The second model is based upon the direct gravitational collapse of massive gas clouds (Loeb & Rasio 1994; Bromm et al. 2009; Volonteri 2010; Latif et al. 2013). Both models include uncertainties and predict markedly different BH growth histories. More exotic scenarios, including BH seed formation via stellar dynamical, rather than gas dynamical processes, have also been suggested(see Volonteri 2010; Bromm & Yoshida 2011 and references therein). These scenarios primarily focus on reproducing the high-redshift quasar population. We must however also be able to explain the existence of less massive and luminous, but more abundant BHs that we find in galaxies such as the Milky Way (Volonteri 2010; Treister et al. 2011). A first step towards constraining seed formation models and determining if they are

★ E-mail: anna.weigel@phys.ethz.ch
† Ambizione Fellow.
‡ Zwicky Fellow.

also valid for such 'normal' BHs, is measuring the BH luminosity function at high redshift.

The *Chandra* 4-Ms catalogue (Xue et al. 2011) provides X-ray counts for the soft (0.5–2 keV), hard (2–8keV) and full (0.5–8 keV) band for the *Chandra* Deep Field South (CDF-S). The on-axis flux limits lie at 9.1×10^{-18}, 5.5×10^{-17} and 3.2×10^{-17} erg s^{-1} cm^{-2} for the soft, hard and full band, respectively. The CDF-S covers a 0.11 deg^2 area. For our analysis, we not only use the *Chandra* 4-Ms data, but also require coverage by the CANDELS wide and deep surveys. The effective area of our field is hence 0.03 deg^2 (Grogin et al. 2011; Koekemoer et al. 2011).[1]

Treister et al. (2013) used the *Chandra* 4-Ms data in their search for high-redshift ($z > 6$) active galactic nuclei (AGN). Using a sample of preselected $z = 6$–8 Lyman Break dropout and photometrically selected sources from the *Hubble* Ultra Deep Field (HUDF) and CANDELS, Treister et al. (2013) showed that none of these sources are detected individually in the X-rays. Stacking the X-ray observations does not produce a significant detection either. Treister et al. (2013) suggested different processes that could account for the lack of X-ray counterparts to these high-redshift sources. The sample could be contaminated by a large number of low-redshift interlopers. A low BH occupation fraction could explain the lack of X-ray counterparts. It is possible that BH growth only occurs in dusty and/or small galaxies which were not included in this analysis because they lie below the detection threshold. The Treister et al. results can also be explained if large amounts of gas and dust obscure the X-ray emission of actively accreting BHs, as previously proposed by Treister, Urry & Virani (2009) and Fiore et al. (2009). Additionally, it is possible that accretion is not the dominant BH growth mode in the early Universe. If BHs are primarily gaining mass by merging with other BHs, X-ray radiation might not probe BH activity. (See Treister et al. 2013 for a more detailed discussion of these possible scenarios.) In addition to the scenarios described above, short, super-Eddington growth episodes, as proposed by Madau, Haardt & Dotti (2014) and Volonteri & Silk (2014), also present a possible solution. In comparison to constant Eddington accretion, the amount of matter that is accreted during these super-Eddington growth phases is the same. However, Madau et al. (2014) showed that, if we allow super-Eddington accretion, a duty cycle of 20 per cent is enough to grow a non-rotating 100 $M_\odot$ seed BH into a 10^9 $M_\odot$ object by $z \sim 7$. One could imagine that the seed BH grows via five 20 Myr long $\dot{m}/\dot{m}_{\rm Edd}$ =four growth modes, each followed by a 100 Myr phase of quiescence. For short, super-Eddington growth episodes, we would thus expect to find fewer BHs that are actively accreting at the same time. The Treister et al. (2013) sample could therefore not contain any BHs that are actively accreting at the time of observation.

In this work, we carefully examine the *Chandra* 4-Ms catalogue for possible $z \gtrsim 5$ AGN. We combine the deep *Chandra* observations with optical and infrared data from GOODS, CANDELS and *Spitzer*. We use the Lyman Break Technique and a photometric redshift code to estimate the redshift of our targets. We also use colour criteria, stacking and the X-ray Hardness Ratio (HR). In contrast to Treister et al. 2013, we base this analysis on detected X-ray sources instead of trying to determine if a high-redshift object possesses a X-ray counterpart. We therefore also analyse X-ray sources that would not be classified as Lyman Break Galaxies because they are heavily obscured in the optical and the infrared.

[1] README for the CANDELS GOODS-S Data Release http://archive.stsci.edu/pub/hlsp/candels/goods-s/gs-tot/v1.0/hlsp_candels_hst_acs-wfc3_gs-tot_readme_v1.0.pdf

We know that the CDF-S contains hundreds of well-constrained $z \gtrsim 5$ Lyman Break Galaxies (see e.g. Stark et al. 2009; Vanzella et al. 2009; Wilkins et al. 2010; Bouwens et al. 2014; Duncan et al. 2014). These should all pass our manual inspection, stacking, colour criteria and photometric redshift measurement. To be considered as a high-redshift AGN candidate, they must however also be detected in the X-rays and pass our X-ray HR test.

Volonteri & Begelman (2010) showed that the expected number density of high-redshift AGN depends on the assumed seed formation model. Both, detection and a non-detection, of high-redshift AGN gives us a lower limit on this number density. Our search thus constrains possible seed formation scenarios and sheds light on BH growth modes.

Vito et al. (2013) searched for $z > 3$ AGN in the 4-Ms CDF-S. They mainly analysed the evolution of obscuration and AGN space density with redshift. In contrast to this work, Vito et al. (2013) based their analysis on already existing photometric and spectroscopic information on the *Chandra* sources. We compare our results to Vito et al. (2013) in Section 5.

This paper is organized as follows. Section 2 describes the data that is used in this work. Sections 3 and 4 introduce our redshift tests and illustrate the results of their combination. We conclude with a discussion in Section 5 and a summary in Section 6. Throughout this paper, we assume a Λ cold dark matter cosmology with $h_0 = 0.7$, $\Omega_{\rm m} = 0.3$ and $\Omega_\Lambda = 0.7$. All magnitudes are given in the AB system (Oke & Gunn 1983).

2 DATA

The *Chandra* 4-Ms source catalogue by Xue et al. (2011) is the starting point of this work. It contains 740 sources and provides counts and observed frame fluxes in the soft (0.5–2 keV), hard (2–8 keV) and full (0.5–8 keV) band. All object IDs used in this work refer to the source numbers listed in the Xue et al. (2011) *Chandra* 4-Ms catalogue. We make use of *Hubble Space Telescope* (*HST*)/Advanced Camera for Surveys (ACS) data from the Great Observatories Origins Deep Survey South (GOODS-south) in the optical wavelength range. We use catalogues and images for filters *F*435*W* (*B*), *F*606*W* (*V*), *F*775*W* (*i*) and 850LP (z) from the second GOODS/ACS data release (v2.0; Giavalisco et al. 2004). We use Cosmic Assembly Near-infrared Deep Extragalactic Legacy Survey (CANDELS) Wide Field Camera 3 (WFC3)/infrared data from the first data release (DR1, v1.0) for passbands *F*105*W* (*Y*), *F*125*W* (*J*) and *F*160*W* (*H*) (Grogin et al. 2011; Koekemoer et al. 2011). To determine which objects are red, dusty, low-redshift interlopers, we also include the 3.6 and 4.5 micron *Spitzer* Infrared Array Camera (IRAC) channels. We use SIMPLE image data from the DR1 (van Dokkum et al. 2005) and the first version of the extended SIMPLE catalogue by Damen et al. (2011).

When comparing *Chandra*, GOODS/ACS and CANDELS object positions, a clear offset in the *Chandra* coordinates is apparent. We illustrate this inconsistency in Fig. 1. To correct for this discrepancy, we calculate the mean displacement between the *Chandra* and the GOODS/ACS catalogue. We determine a mean offset of $\mathrm{RA}_{Chandra} - \mathrm{RA}_{\rm ACS} = 0.128$ arcsec and $\mathrm{Dec.}_{Chandra} - \mathrm{Dec.}_{\rm ACS} = -0.237$ arcsec. We adjust the GOODS/ACS and CANDELS positions of each object by subtracting the mean displacement from the originally given catalogue position.

3 ANALYSIS

In the following section, we describe in detail the set of criteria we employed to the data in order to identify $z \gtrsim 5$ candidates. We first

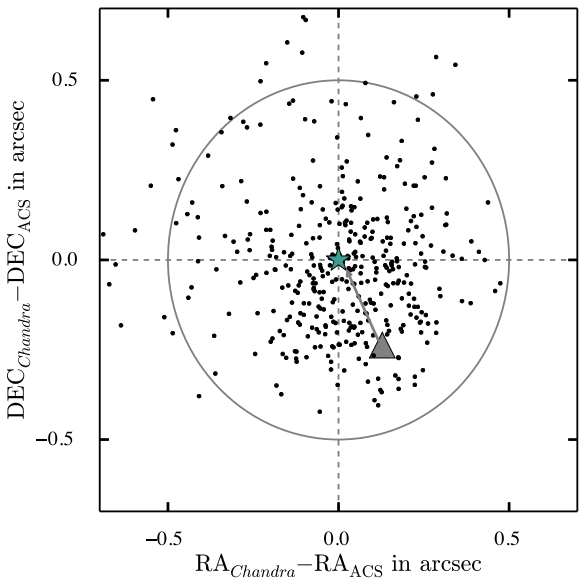

Figure 1. Offset between GOODS/ACS and *Chandra* positions after the correction has been applied. Out of the 740 *Chandra* X-ray sources, 408 possess an optical counterpart. We determine a mean offset of (0.128 arcsec, −0.237 arcsec) for these 408 objects and correct for it by shifting the *Chandra* positions. The grey triangle indicates the mean displacement before the correction. The green star illustrates the mean offset after our correction. The black points show the corrected object positions. The grey circle illustrates an offset of 0.5 arcsec.

exclude objects with insufficient filter coverage, perform our own aperture photometry and determine the dropout band of each source by manual inspection. We run a photometric redshift code, stack the GOODS/ACS data and apply colour criteria. In addition, we use the X-ray data as a photometric redshift indicator. We combine all redshift tests in Section 4. Fig. 2 illustrates and summarizes the complete analysis that is detailed in the following subsections.

Dahlen et al. (2010), McLure et al. (2011) and Duncan et al. (2014) showed that when selecting high-redshift objects, a selection based only on colour criteria is not as reliable as calculating photometric redshifts. Especially for faint, low signal-to-noise objects, errors and upper limits can lead to scattering out of the colour selection region. Similar to colour criteria, photometric redshifts strongly depend on the position of the Lyman Break. A photometric redshift code does however consider all filter information, including upper limits and errors. Furthermore, low-redshift interlopers can be identified by including the filters redward of the Lyman Break. Dahlen et al. (2010) illustrated the discrepancy between colour criteria and photometric redshifts for the GOODS-S field. Only 50 per cent of their photometrically selected $z \sim 4$ sources were also classified as *B* dropouts according to colour criteria. We therefore primarily use a photometric redshift code. The colour criteria, our visual classification, the stacking of the GOODS/ACS data and the X-ray HR provide additional redshift indications.

3.1 Initial sample selection

Our initial sample consists of the 740 objects given in the *Chandra* 4-Ms source catalogue. Fig. 3 shows that not all *Chandra* targets are covered by the GOODS/ACS and CANDELS images. However, adjacent filter coverage is necessary for the application of the Lyman Break Technique. We therefore narrow the number of possible candidates down to 374 by removing sources that are not covered by *B*, *V*, *i*, *z*, *J* and *H*. The *Y*-band area is small compared to the other filters. We therefore also include sources that are not covered by the *Y*-band provided that they are covered by all other GOODS/ACS and CANDELS filters. The optical and infrared counterpart detection is primarily based upon the *H*-band image since this is the deepest band. The *H*-band images for objects 105 and 521 show significant artefacts, we therefore discard them. Source 366 is eliminated due to the object's position being at the edge of the GOODS/ACS images. Hence, 371 possible candidates remain after this first visual preselection.

3.2 Aperture photometry

We perform our own aperture photometry on the GOODS/ACS and CANDELS images to gain flux values and to estimate parameters such as detection threshold and aperture size. We compare our results to the GOODS/ACS catalogue (Fig. 4).

To perform aperture photometry, we use Source-Extractor (SExtractor; Bertin & Arnouts 1996; Bertin et al. 2002; Holwerda 2005). We determine the counterpart position in the *H* band in a first SExtractor run. We then run SExtractor on the remaining optical and infrared images to establish if the counterpart is present at the same location. The flux measurements are carried out within circular apertures with radii between 0.3 arcsec and 1 arcsec. We alter the aperture size for faint sources and to prevent contamination through nearby objects. For sources with a signal-to-noise ratio <1, we use the 1σ sensitivity limit of the corresponding filter as an upper limit. The SExtractor parameter values and aperture sizes are summarized in Table A1 and Table A2. For the 3.6 micron and 4.5 micron bands, we rely on the flux values reported in the SIMPLE catalogue (Damen et al. 2011). We make use of the flux values reported for a 1.5 arcsec radius aperture. We show flux and error values for our main sample in Tables A5 and A6.

3.3 Lyman break technique and visual classification

The Lyman Break Technique (Steidel et al. 1999; Giavalisco 2002; Dunlop 2013) employs the pronounced feature of the Lyman continuum discontinuity in the spectral energy distribution (SED) of young, star-forming galaxies. We use the common terminology of referring to Lyman Break Galaxies as 'dropouts'. If a source is not detected in the *B* band or any bluer passbands, but is visible in all redder filters, this indicates $z \sim 4$ and we refer to it as a '*B* dropout'. *V*, *i* and *z* dropouts correspond to redshifts of ∼5, ∼6 and ∼7, respectively.

We classify the 371 possible candidates by eye according to their dropout band. If an object is clearly visible in all bands, this indicates $z < 4$. We exclude such sources from our sample. Fig. 5 illustrates the conditions sources have to fulfil to be included in the further analysis.

Eight sources are not classified according to their dropout band. These objects are shown in Figs 6 & 7 shows the hard and soft band counts for all eight sources in comparison to the entire sample. The hard, soft and full band counts are given in Table 1.

Five (190, 280, 333, 384, 643) of these eight objects are especially interesting since they do not have a counterpart in the optical or the infrared. We refer to these sources as *'low-significance objects'*. We show these five objects in the upper panel of Fig. 6. For three (104, 156, 276) of these eight objects, it is unclear which source represents the counterpart in the optical and infrared since multiple objects are visible in the GOODS/ACS and CANDELS bands. These objects are shown in the lower panel of Fig. 6.

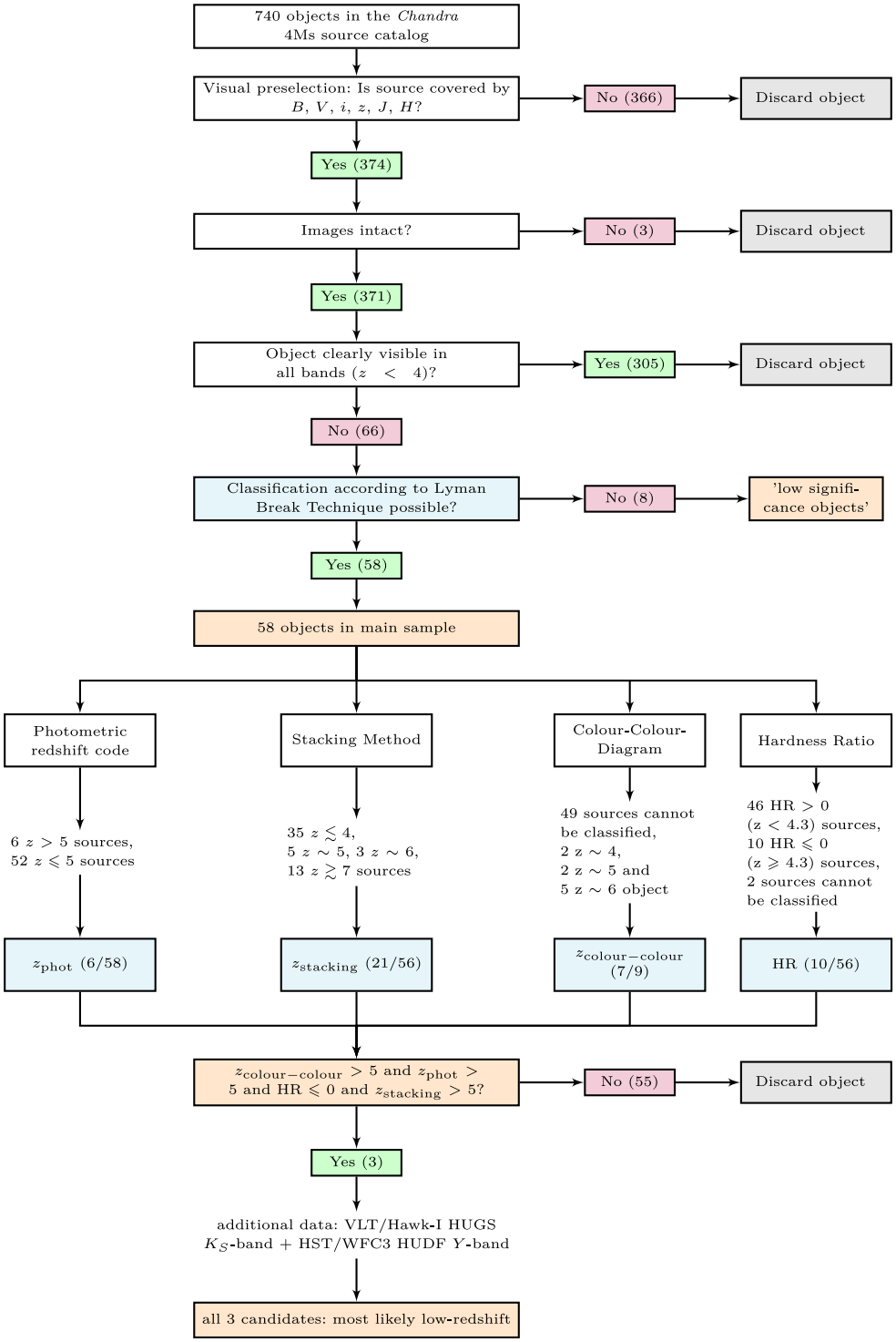

Figure 2. Flowchart illustrating the analysis steps that we take to determine possible $z \gtrsim 5$ candidates. The number of objects that pass each step is given in brackets. After executing this analysis for all 740 *Chandra* sources, three $z \gtrsim 5$ candidates remain in our sample. Additional K_S-band and deep Y-band data does however show that they are most likely low-redshift sources.

Only three of the eight objects (333, 156, 276) are detected in the full, the hard and the soft band. 104 and 280 are detected in the soft band only. 384 and 643 are found in the soft and in the full band. 190 is detected in the full band only. Only one of the low-significance objects (333) and one of the three sources with multiple counterparts in the optical and infrared (156) show a signal-to-noise ratio $\geq$5 in at least one of the bands. Out of the 371 objects with enough filter coverage and intact images 140 (37.7 per cent) have a signal-to-noise ratio $\geq$5 in the soft, hard or full band. See Table A3 for the number of sources with signal-to-noise ratios $\geq$1 and $\geq$5 in the individual bands.

The objects for which we do not detect a counterpart in the optical and the infrared could be spurious detections. On the one hand, Xue et al. (2011) report that, for the entire catalogue, the probability

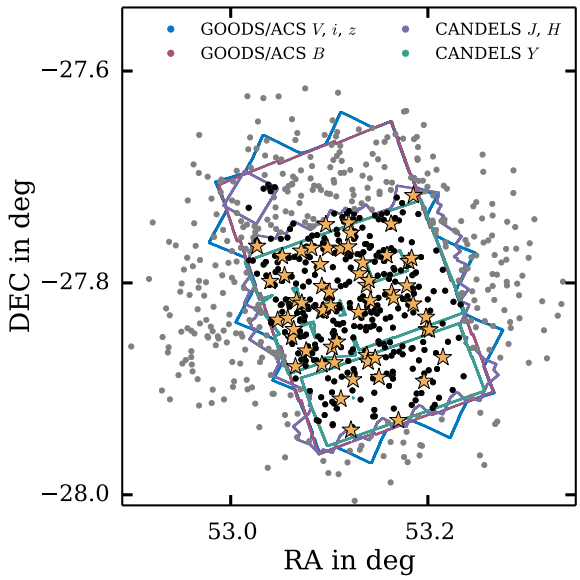

Figure 3. Overview of the area covered by the *HST*/ACS filters *B* (red), *V*, *i*, *z* (blue), the *HST*/WFC3 bands *Y* (green), *J*, *H* (purple) and our 740 *Chandra* 4-Ms sources. Grey points mark sources that are not of interest for this work because they are not covered by enough bands (*B*, *V*, *i*, *z*, *J*, *H*) to use the Lyman Break Technique. Black points indicate objects with enough filter coverage that were eliminated because the objects are clearly visible in all bands. According to the Lyman Break Technique, this indicates $z < 4$. Yellow stars mark the positions of the 58 potential high-redshift AGN that we analyse more closely.

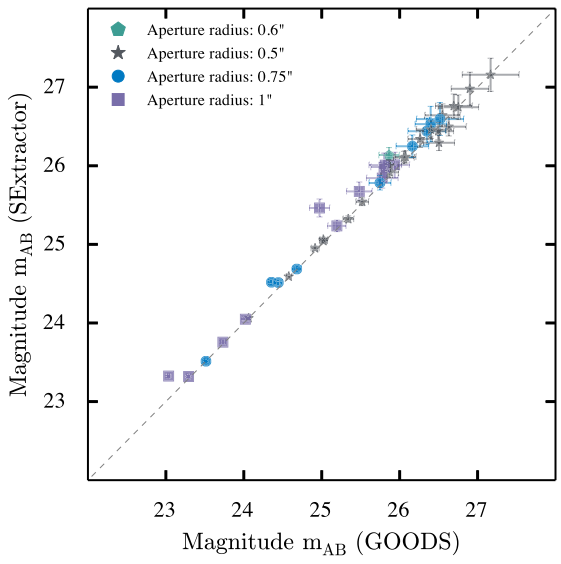

Figure 4. Comparison between our own photometry and the flux values reported in the GOODS catalogue (Giavalisco et al. 2004). We show the AB magnitude values for the *z* band. Note that the GOODS/ACS catalogue only contains flux values for an aperture with a 0.707 arcsec and not a 0.75 arcsec radius. Nonetheless, we compare these values to the brightness we measured within a 0.75 arcsec radius aperture. We use a small 0.3 arcsec radius aperture for two objects only. Since these two sources are not detected in the GOODS/ACS catalogue, they are not part of this comparison.

of a source not being real is <0.004. The entire catalogue does therefore contain up to three spurious sources per band. We do however only consider sources that are also covered by GOODS and CANDELS. The CANDELS wide and deep survey fields are 0.03 deg^2 in size and hence only make up ∼27 per cent of the CDF-S (0.11 deg^2) area. According to this, we would expect to find ∼0.8 spurious detections per band. So, we can-not rule out the fact that we may have found one or more false detections. On the other hand, we find many sources of comparable X-ray brightness that do possess an optical and/or infrared counterpart and that are detected in both bands (Fig. 7). 333, 384 and 643 are also close to a bright galaxy which might be why the counterpart remains undetected. This could indicate that at least some of the sources are real.

The Lyman Break Technique is not applicable to the low-significance objects and we are unable to measure a photometric redshift without a detection in the optical and the infrared. Since 333 is detected in the hard and the soft band, it is the only object for which we can apply our HR test (see Section 3.7). With HR = −0.01 333 could be a potential high-redshift AGN candidate. A negative HR alone does however not convince us of 333 indeed being at high redshift. At this point, we can thus not determine if our sources are real high-redshift AGN candidates, false detections or low-redshift objects that are optically faint. Hopefully, the forthcoming 7-Ms observations of the CDF-S (PI: William Brandt, Proposal ID: 15900132) will shed more light on our five low-significance objects. We eliminate all eight sources from our sample. We stress that these targets could still be high-redshift AGN.

After discarding targets that are clearly visible in all bands and eliminating the eight objects that could not be classified according to the Lyman Break Technique, 58 *B*, *V*, *i*, *z* and *Y* dropouts remain in our main sample. For sources that we visually classify as *B* dropouts, the signal to noise in the *V* band might be too low for a detection by SExtractor. By eliminating visually classified *B* dropouts, we could hence be missing objects that might be classified as $z \sim 5$ sources by other redshift tests. We therefore keep *B* dropouts in our sample.

3.4 Photometric redshift measurements

Even though the Lyman Break Technique provides a fast and easy way of identifying possible candidates, it is not without caveats. Dust in red, low-redshift galaxies can produce a sharp break in the SED that might be mistaken for the Lyman Break (Dunlop, Cirasuolo & McLure 2007; McLure et al. 2010; Finkelstein et al. 2012). Applying the Lyman Break Technique therefore only produces a sample that may still contain low-redshift interlopers. Yet, even the results of a photometric redshift code have to be treated carefully. While sources with a low photometric redshift are most likely indeed nearby objects, high photometric redshift results are less reliable. This is mainly due to template incompleteness and large photometric errors for faint high-redshift sources.

The photometric redshifts we determine for our objects prove to be highly dependent on the filters used as input. We use the photometric redshift code EAZY (Brammer, van Dokkum & Coppi 2008). We apply the default template set by Brammer et al. (2008) which is part of the EAZY distribution. Five of these six EAZY templates were created by using the Blanton & Roweis (2007) algorithm to reduce the template set by Grazian et al. (2006). The sixth template describes a young starburst with a dust screen following the Calzetti law with $A_v = 2.75$ (Calzetti et al. 2000). Due to large uncertainties in the luminosity function of high-redshift AGN, we do not include a luminosity prior when running EAZY. To gain reliable redshift values, we take the *Spitzer*/IRAC images into account. We carefully compare the *H*-band CANDELS images to the *Spitzer* 3.6 micron images to determine which of our candidates possesses a *Spitzer*

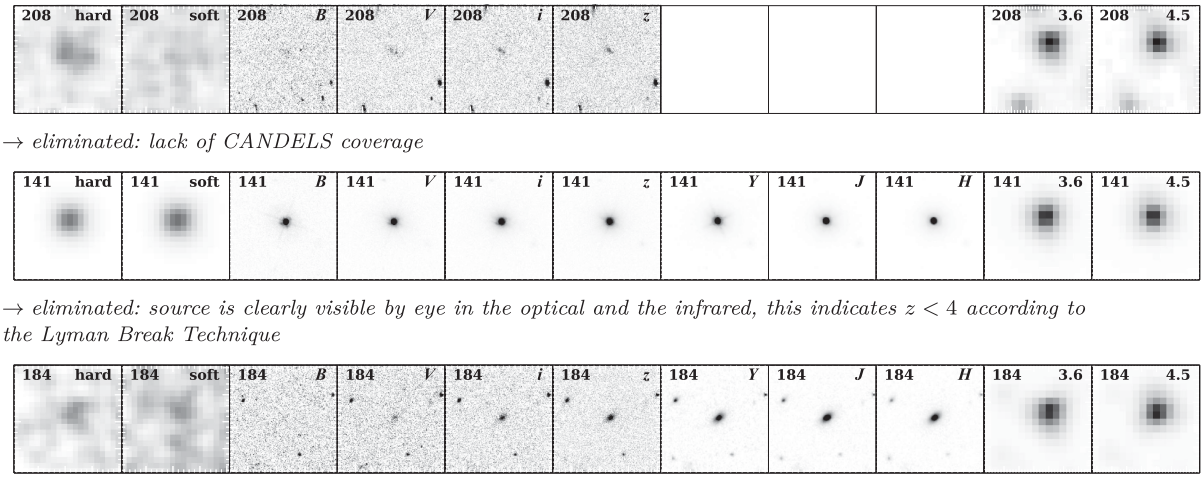

Figure 5. Classification examples. We only kept source 184 in our sample. The images are 10 arcsec × 10 arcsec in size and were colour inverted.

counterpart and for which sources the *Spitzer* flux values cannot be used due to source confusion. We include the *Spitzer* images for 30 of our 58 objects. We show the *H* band and *Spitzer* stamps for these sources in the appendix. We do not perform aperture photometry on the *Spitzer* images, but simply extract the 1.5 arcsec aperture radius flux values from the *Spitzer* catalogue by Damen et al. (2011).

If a source is not detected in a passband, we use the 1σ sensitivity limit of this filter as an upper limit in the EAZY run. For the GOODS/ACS bands B, V, i and z, we determine the sensitivity limits by measuring the mean background flux. We measure the number of background counts for six of our objects. For each source, we determine the flux within apertures of varying size at five different positions. For the CANDELS bands Y, J and H, we rely on the sensitivity limits reported in Grogin et al. (2011). Table 2 shows the flux limits that we used in our analysis.

Including the *Spitzer* data turns out to be crucial for our purposes. As an example, we show the photometric redshift code results we get for source 244 in Fig. 8. By running EAZY without the *Spitzer* flux values, we gain $z_{\rm phot} = 6.54$. Assuming that this photometric redshift value is correct, we determine an absolute magnitude of $M_H = -24.63$ for the H-band. Bouwens et al. (2014) however give $M^*_{\rm UV} = -21.2$ for $z \sim 6$ Lyman Break Galaxies. 244 would therefore be very bright if it indeed was at $z \sim 6$. Including the 3.6 and 4.5 micron *Spitzer* flux values in the photometric redshift code analysis results in $z_{\rm phot} = 1.9$. Including the *Spitzer* infrared data hence proves to be crucial in revealing low-redshift interlopers.

3.5 Stacking GOODS/ACS data

We combine the GOODS/ACS images of each object into stacks. We generated three stacks per source: (1) combines B and V, (2) B, V and i and (3) B, V, i, z. We examine these deeper stacks for detections by running SEXTRACTOR on them. We use a detection threshold of 1.5σ (DETECT_TRESH = 1.5) and a minimum detection area of 15 pixels above the threshold (DETECT_MINAREA = 15). The remaining SEXTRACTOR parameter values are left at their default values. A detection in the first stack indicates a source that drops out before or in the B band and therefore implies $z \lesssim 4$. Sources that are detected in (1), (2) and (3) are hence of no interest to us. We assume $z \sim 5$ if an object is detected in (2) and (3), but not in (1). Only being detected in (3) indicates $z \sim 6$. Finally, no detection in any stack signals $z \gtrsim 7$. Using this approach, we find 35 $z \lesssim 4$, 5 $z \sim 5$, 3 $z \sim 6$ and 13 $z \gtrsim 7$ sources. The stacking analysis proves to be inconclusive for two objects (303, 651). Source 303 is detected in (1) and (3), but not in (2). 651 is only found in stack (2).

3.6 Colour criteria

We obtain an additional redshift indication by applying colour criteria based upon population synthesis models (Guhathakurta, Tyson & Majewski 1990; Steidel & Hamilton 1992). These colour criteria do not only depend on the position of the Lyman Break, but also use the overall SED shape. The criteria we apply here are based on Vanzella et al. (2009) who used 114 Lyman Break Galaxies from the GOODS field. The sample consisted of 51 $z \sim 4$, 31 $z \sim 5$ and 32 $z \sim 6$ Lyman Break Galaxies. These objects were first chosen by applying the Lyman Break Technique and then followed up spectroscopically.

Objects that fulfil the following condition are classified as $z \sim 4$ sources:

$$(B - V) \geq (V - z) \wedge (B - V) \geq 1.1 \wedge (V - z) \leq 1.6. \quad (1)$$

Here, $\wedge$ and $\vee$ represent the logical 'and' and 'or' operators, respectively. $z \sim 5$ objects need to satisfy the constraints given here:

$$[(V - i) > 1.5 + 0.9 \times (i - z)] \vee [(V - i) > 2.0] \wedge$$
$$(V - i) \geq 1.2 \wedge (i - z) \leq 1.3 \wedge (\mathrm{S/N})_{\rm B} < 2. \quad (2)$$

For $z \sim 6$ galaxies these conditions apply:

$$(i - z) > 1.3 \wedge [(\mathrm{S/N})_{\rm B} < 2 \vee (\mathrm{S/N})_{\rm V} < 2]. \quad (3)$$

To classify the 58 possible candidates according to colour criteria, we use the magnitude values from our aperture photometry (see 3.2). If a source is not detected, we use the 1σ sensitivity limit as an upper limit. 49 of the 58 sources do not fulfil any colour criteria. Note that a source that simultaneously possesses upper limits in the B and V or V and z band is not included in the $z \sim 4$ diagram since its position cannot be determined. The same applies for the $z \sim 5$ and $z \sim 6$ diagrams. Furthermore, we only use colour criteria to determine $z \sim 4$, $z \sim 5$ and $z \sim 6$ dropouts. The 49 objects that cannot be classified are hence not all necessarily at $z < 4$. Fig. A1 shows the colour–colour diagrams that illustrate these criteria. Based on

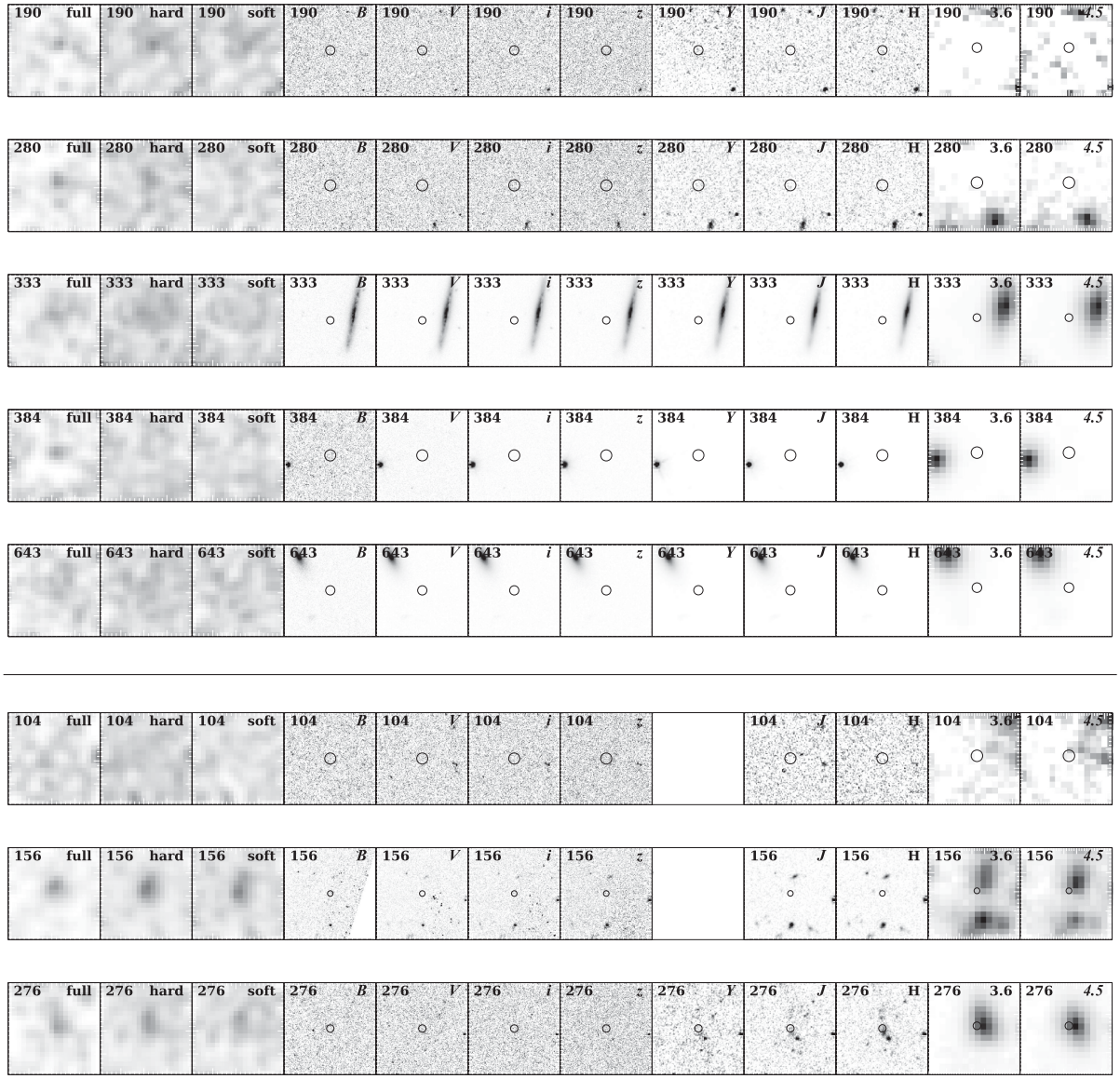

Figure 6. Sources that cannot be classified according to their dropout band. Top: sources that are in the *Chandra* 4-Ms catalogue but do not show a clear counterpart in the optical and infrared, *'low-significance objects'*. 333, 384 and 643 are close to a bright galaxy which is why we might not be able to detect the counterpart in the optical and infrared. Deeper observations would be needed to detect possible counterparts. Bottom: sources with multiple possible counterparts. Out of these eight objects only 156, 276 and 333 are simultaneously detected in the hard and in the soft band. We are unable to gain redshift estimates for these eight objects and are thus unable to determine if they are low or high-redshift sources or if they might be spurious detections. The black circles are centred on the original *Chandra* position and illustrate the positional uncertainty given in the Xue et al. (2011) catalogue. All images were colour inverted and are 10 arcsec $\times$ 10 arcsec in size.

colour criteria, we find 2 $z \sim 4$ (373, 444), 2 $z \sim 5$ (303, 321) and 5 $z \sim 6$ (226, 244, 296, 522, 589) objects.

3.7 X-rays as a photometric redshift indicator

The HR, sometimes denoted as X-ray colour, represents an additional indicator for high-redshift AGN. The HR is defined as

$$\mathrm{HR} = \frac{\mathrm{H} - \mathrm{S}}{\mathrm{H} + \mathrm{S}}. \quad (4)$$

Here, H and S represent the observed frame hard (2–10 keV) and soft (0.5–2 keV) band counts, respectively.

To zeroth-order, an AGN X-ray spectrum follows a power law with an obscuration dependent turnover at lower energies. In the Compton-thin regime, a higher column density N_{H} means that, relative to the hard band, we will detect fewer counts in the soft band. In a galaxy's restframe, the X-ray spectrum hence appears harder for higher obscuration. With increasing redshift, the spectrum gets shifted to lower energies and the number of counts that we observe in the hard and in the soft band changes accordingly. We can therefore use the HR as an additional redshift indicator.

A soft X-ray spectrum is then expected for Compton-thin ($N_{\mathrm{H}} < 10^{24}\,\mathrm{cm}^{-2}$) objects. For sources in which $10^{24} \lesssim N_{\mathrm{H}}$ H $\lesssim 10^{25}\,\mathrm{cm}^{-2}$, i.e. transmission-dominated Compton-thick AGN, the direct emission is still visible, although the E < 10 keV radiation is completely obscured by photoelectric absorption, while the detected emission at higher energies is reduced by Compton scattering (Murphy & Yaqoob 2009; Comastri et al. 2010). Hence,

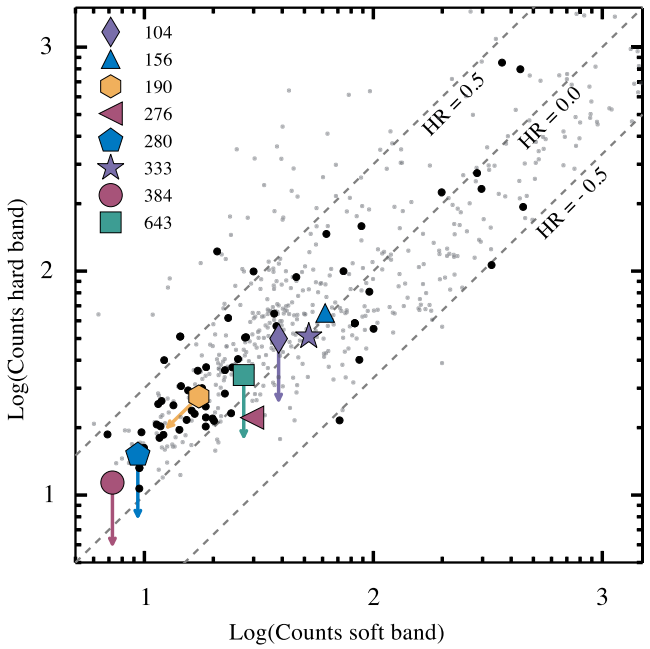

Figure 7. Counts in the hard and in the soft band for the *Chandra* 4-Ms sources. We highlight the eight objects that could not be classified according to the Lyman Break Technique. These eight sources might be real sources or spurious detections. The black points illustrate the 58 objects that are left in our sample. The grey points show the positions of the additional 502 *Chandra* 4-Ms objects that are also classified as AGN. They were excluded because of insufficient filter coverage or quality or because they are clear low-redshift dropouts. Xue et al. (2011) categorize all of these eight objects and all 58 sample sources as AGN.

in these cases we expect to observe a hard X-ray spectrum even for sources at $z > 5$. When $N_{\rm H} > 10^{25}\,{\rm cm}^{-2}$, i.e. for reflection-dominated Compton-thick AGN, we only observe the small fraction of the initial emission which is reflected off the accretion disc or the obscuring material (Ajello 2009; Brightman & Nandra 2012). We can hence not make the same assumptions as for Compton-thin sources. Nevertheless, it is safe to assume that all $z \gtrsim 5$ sources that can be detected individually in the X-rays are Compton-thin objects. Compton-thick $z \gtrsim 5$ AGN would simply be too faint to be detected individually and are therefore not part of our sample.

To quantify the HR(z) relation, we use the X-ray spectral fitting tool XSPEC to simulate X-ray spectra at different redshifts (Arnaud 1996). We use a `zphabs*zpow` model and assume a power-law slope of 1.8 (Turner et al. 1997; Tozzi et al. 2006). Fig. 9 summarizes our results. The left-hand panel illustrates our model for $N_{\rm H} = 10^{22}$, $10^{22.5}$ and $10^{23.5}\,{\rm cm}^{-2}$ (blue, yellow and green, respectively) at $z = 0.1$, 3 and 6 (dot dashed, solid and dashed line, respectively). It is evident that the number of counts in the soft and hard band changes with redshift. After including the *Chandra* Redistribution Matrix (RMF) and Auxiliary Response Files (ARF) for on-axis sources, we measure the spectral counts in the hard and in the soft band and determine the HR. The right-hand panel of Fig. 9 shows our results. According to our simulations, HR > 0 signifies $z < 4.34$ for sources with $N_{\rm H}$ up to $10^{23.5}\,{\rm cm}^{-2}$. Allowing for a small amount of transmission, e.g. 1 per cent by using a `zpcfabs*zpow` model does not change our results significantly (HR $= 0$ for $z = 4.3$). In our analysis, we hence discard objects with HR > 0. Fig. 10, which illustrates our results, shows that based solely on the HR, 10 of our 58 candidates might be at $z > 4.34$. For 496 and 583, the HR cannot be used to constrain z since they are only detected in the full band. Table A4 summarizes the X-ray counts, signal-to-noise ratios and HRs for each of our main sample sources.

Our results are in good agreement with a similar analysis by Wang et al. (2004). They also used XSPEC (Arnaud 1996) to simulate the HR at different redshifts. Yet, Wang et al. (2004) chose a power-law slope of 1.9 and used a `wabs` model. Our analysis shows that $z > 5$ sources with $N_{\rm H}$ up to $10^{23}\,{\rm cm}^{-2}$ should have an HR of ~ -0.3, Wang et al. (2004) find HR~ -0.5. For $N_{\rm H} = 10^{23}\,{\rm cm}^{-2}$, we determine HR $= 0$ at $z \sim 2$, Wang et al. (2004) find HR $= 0$ at $z \sim 1.5$.

Table 2. GOODS/ACS flux limits. We determine these mean sensitivity limits by measuring the mean background flux for six different objects. For each object, we determine the background counts within five apertures of varying size.

	1σ flux limit in μJy/arcsec^2
B	4.636×10^{-2}
V	4.160×10^{-2}
i	8.255×10^{-2}
z	1.487×10^{-2}

4 COMBINING ALL REDSHIFT TESTS

We now combine our stacking, colour criteria and photometric redshift code results. Table 3 summarizes the redshift test results. Table 4 provides all redshift values and object positions. We exclude objects with $z_{\rm phot} < 5$, $z_{\rm stacking} < 5$ and $z_{\rm colour} < 5$. Without the HR constraint six $z > 5$ objects remain (Fig. 11). Neither stacking,

Table 1. Hard, soft and full band counts for sources that cannot be classified according to their dropout band. We refer to the top five sources as 'low-significance objects'. For objects that are not detected we give an upper limit on the counts. We set σ to -1.00 and mark the signal-to-noise ratio with a dash. All values were directly extracted from the *Chandra* 4-Ms catalogue (Xue et al. 2011).

ID	Hard counts	$\sigma_{\rm Hard}$	SNR$_{\rm Hard}$	Soft counts	$\sigma_{\rm Soft}$	SNR$_{\rm Soft}$	Full counts	$\sigma_{\rm Full}$	SNR$_{\rm Full}$
190	27.55	−1.00	–	17.29	−1.00	–	21.99	10.12	2.17
280	15.13	−1.00	–	9.36	4.94	1.89	18.36	−1.00	–
333	51.15	16.91	3.02	52.23	11.59	4.51	103.21	19.66	5.25
384	11.37	−1.00	–	7.25	4.44	1.63	14.98	−1.00	–
643	34.34	−1.00	–	27.16	8.72	3.11	33.54	13.21	2.54
104	49.95	−1.00	–	38.57	12.16	3.17	57.78	−1.00	–
156	65.01	13.43	4.84	61.59	10.59	5.82	126.33	16.40	7.70
276	22.17	9.54	2.32	29.55	7.95	3.72	51.61	11.70	4.41

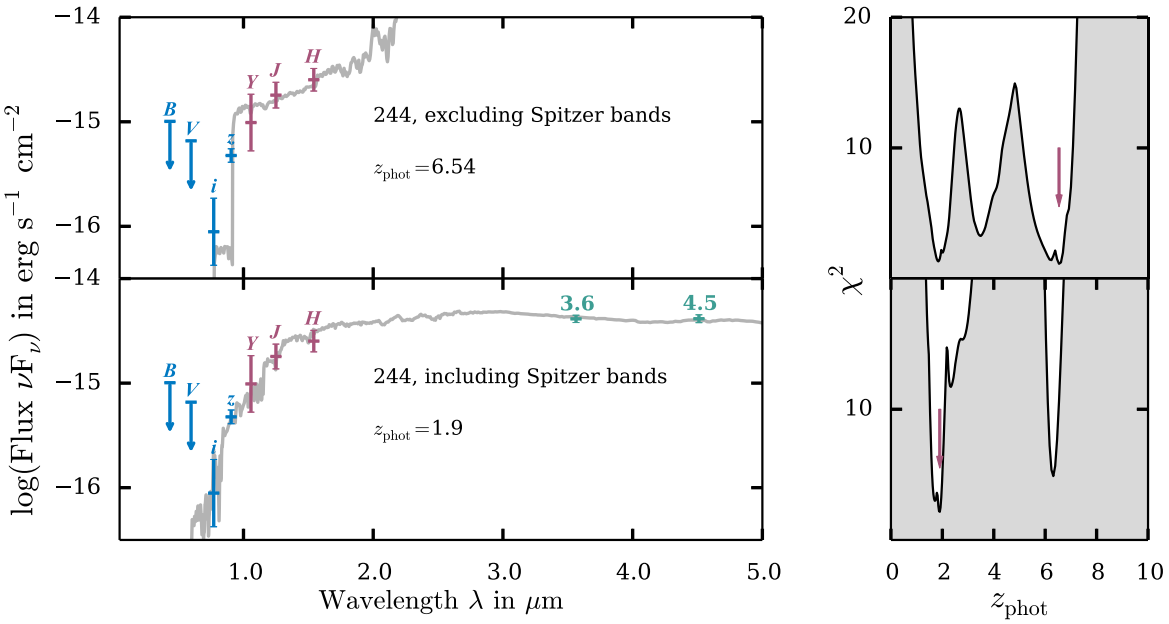

Figure 8. Best-fitting SED for 244 determined by running EAZY without the *Spitzer* data (*top*) and with the *Spitzer* data (*bottom*). If we only use the GOODS/ACS and CANDELS filters as input for EAZY, the photometric redshift code will classify 402 as a $z \sim 6.54$ source. Even though the flux values are fit well by this SED, the shape of the SED seems unphysical for a $z \sim 6.54$ source. We would expect the continuum flux to be lower and bluer. A comparison to the $z \sim 7$ UV luminosity function by Bouwens et al. (2014) shows that 244 would indeed be bright if it was at $z \sim 6.54$ ($M_H = -24.6$). The χ^2 distribution on the right shows multiple secondary low-redshift solutions. SED shape and χ^2 distribution thus suggest that 244 might be a low-redshift object. In the bottom panel, we illustrate the best-fitting SED determined by including the *Spitzer* 3.6 and 4.5 micron IRAC channels. 244 is now exposed as a low-redshift source. Based upon $z \sim 1.9$, we reject 244 as a possible high-redshift candidate. The shown limits correspond to the 1σ sensitivity limits.

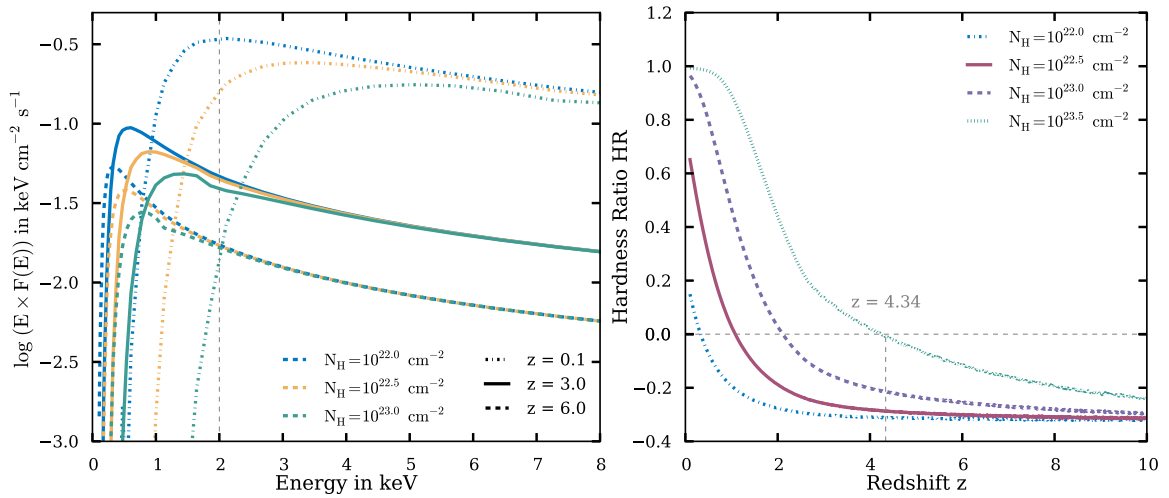

Figure 9. AGN X-ray spectrum simulation. Shown on the *left* is our model that we generated by running XSPEC (Arnaud 1996). We assume a power law with a slope of 1.8 and a turnover due to photoelectric absorption (XSPEC `zphabs*zpow` model). This left-hand plot illustrates the model SED for moderately high column densities (line colours) at several redshifts (line types). With increasing redshift, the spectrum gets shifted to lower energies and the number of counts in the hard and in the soft band changes. Right: measured HR as a function of redshift (HR $= \frac{\rm H-S}{\rm H+S}$, H and S representing the counts in the hard and in the soft band, respectively). Based on our model, a HR > 0 indicates $z < 4.34$ for column densities up to $N_{\rm H} = 10^{23.5}$ cm^{-2}. In our analysis, we thus dismiss objects with an HR > 0 as obscured AGN at low redshift.

colour criteria nor our visual classification contradict $z > 5$ for these six sources (226, 371, 456, 578, 583, 430). For 371, 456, 578, 583 and 430, the 1σ error bars on $z_{\rm phot}$ are asymmetric and reach below $z \sim 5$. The χ^2 distributions (Fig. 11) also do not show clear global minima. For 430 and 578, the χ^2 distributions are flat and allow for a wide range of lower redshift solutions. The $z_{\rm phot}$ solution for 456 is at the upper end of our allowed $z_{\rm phot}$ range ($z_{\rm phot} = 0$–11). 371 shows additional minima at $z_{\rm phot} \sim 1$. For 226, we determine an absolute magnitude of $M_H = -25.6$ assuming a photometric redshift of 5.43. 226 would therefore be extremely bright if it indeed was at $z \sim 5$ (see section 3.4). There is thus only little evidence supporting the fact that these objects might be at high redshift. Only 226, 456 and 583 show global minima and are thus our most promising candidates.

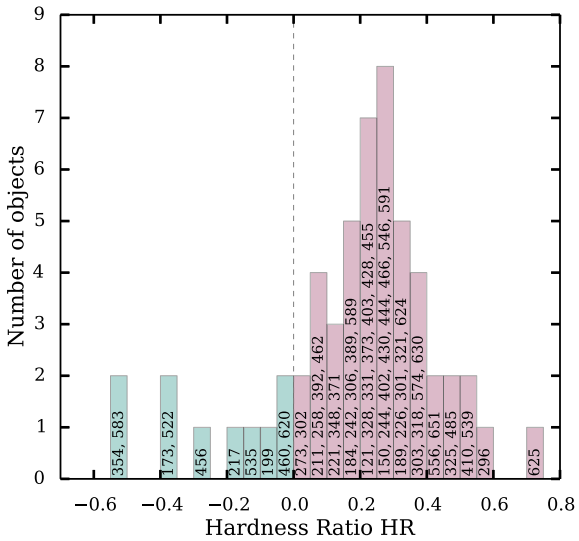

Figure 10. Number of objects per HR bin. This figure illustrates the distribution of our 54 objects in terms of HR. HR < 0 indicates that this source might be at $z > 4.34$. A positive HR suggests that this source might be at $z \leq 4.34$. Thus 10 of our 54 objects might be at $z > 4.34$. Not shown are objects 496 and 578. These two sources are only detected in the full band and can therefore not be constrained by the HR. The numbers in each bar coincide with the object IDs in the corresponding HR bin.

4.1 Our three final candidates

We now also take the HR information into account and exclude three of the six remaining sources based on a positive HR value. After combining all of our redshift tests we are hence left with three final high-redshift candidates (456, 578, 583, Fig. 12). 456 and 583 have a negative HR whereas 578 cannot be constrained by HR since it is only detected in the full band.

For 456, we find $z_{\rm phot} = 10.91^{-0.92}_{-8.39}$ ($\chi^2 \sim 0$) and HR $= -0.29$. For 578, we determine $z_{\rm phot} = 6.77^{+0.97}_{-5.10}$ ($\chi^2 \sim 0$). 583 has HR $= -0.51$ and $z_{\rm phot} = 9.36^{+0.63}_{-4.82}$ ($\chi^2 \sim 0$). 456, 578 and 583 could not be classified according to our colour criteria. Nonetheless, our visual classification (z dropouts) and our stacking analysis ($z_{\rm stacking} \sim 7$ for all) indicate that these sources might be $z > 5$ AGN.

4.2 Expected number densities

We note that 456, 578 and 583 seem bright for $z \sim 7$ and $z \sim 10$ sources. We use UV rest-frame galaxy luminosity functions by Bouwens et al. (2014) to quantify this statement. To justify our comparison to the galaxy, and not quasar luminosity function, we calculate $\alpha_{\rm ox}$ for our candidates. $\alpha_{\rm ox}$, the X-ray to optical-UV ratio, is defined as $\alpha_{\rm ox} = \log[L_{2500\,\text{Å}}/L_{2\,\text{keV}}]/2.605$ (e.g. Tananbaum et al. 1979; Wilkes et al. 1994; Vignali, Brandt & Schneider 2003; Steffen et al. 2006). Lusso et al. (2010) analyse a sample of 545 X-ray selected Type 1 AGN from the *XMM*-COSMOS survey and find a mean $\alpha_{\rm ox}$ value of $\sim$1.37 and a weak redshift dependence out to $z \sim 4$. We use the H-band and soft band flux values to calculate $\alpha_{\rm ox}$ for 456, 578 and 583. We find $\alpha_{\rm ox} = 0.11$, 0.35 and -0.02 for 456, 578 and 583, respectively. Assuming that $\alpha_{\rm ox}$ has no strong redshift dependence for $z > 4$, this indicates that 456, 578 and 583 are not high-redshift quasars and justifies our comparison to the results by Bouwens et al. (2014).

We estimate the number of sources similar to 456, 578 and 583 that we expect to find in our field. Since we only analyse objects for which GOODS/ACS and CANDELS data is available, we are only considering the area of the CANDELS deep and wide surveys (0.03 deg^2) and not the entire CDF-S (0.11 deg^2). Based on the surface density of $z \sim 7$ and $z \sim 10$ galaxies by Bouwens et al. (2014), we expect to find 0.14 ± 0.14 sources as bright as 456 at $z \sim 10$, 3.72 ± 0.80 objects similar to 578 and less than 0.15 $z \sim 10$ objects as bright as 583. We hence expect high-redshift sources as bright as 456, 578 and 583 to be rare.

4.3 Deeper *Y*-band imaging for 583

583, one of our three final candidates, has a high photometric redshift ($z_{\rm phot} = 9.36$) and shows a clear global minimum in the χ^2 distribution. In terms of the χ^2 distribution, it is thus our most promising candidate. Fortunately, 583 is part of the HUDF (Beckwith et al. 2006). We are especially interested in deeper Y-band imaging since 583's high photometric redshift hinges on the upper limit in this band. We show our results in Fig. 14. The top panels illustrate, that the upper limit in the Y band, for which we used the official sensitivity limit given by Grogin et al. (2011), is very low and thus forces a strong break in 583's SED. We hence combine all available *HST*/WFC3 HUDF Y-band images (Koekemoer et al. 2013, *HST* Program ID 12498, PI: R. Ellis; Illingworth et al. 2013, *HST* Program ID 11563, PI: G. Illingworth, *HST* Program ID 12099, PI: A. Riess) using the *HST* DRIZZLEPAC package. We measure the flux of 583 using simple aperture photometry and a 0.3 arcsec radius aperture (middle panels) and rerun EAZY. We use the $\Delta\chi^2$ method under the assumption of one free parameter ($z_{\rm phot}$) to compute the 1σ, 2σ and 3σ error bars. We still determine a high photometric redshift of $z_{\rm phot} = 7.41$, a low-redshift solution at $z_{\rm phot} \sim 2$ is however allowed within 1σ. 583 is hence unlikely to be at high redshift.

4.4 HUGS $K_{\rm S}$-band data

To gain more reliable photometric redshift values for all three of our final candidates, we now also take Very Large Telescope (VLT)/High Acuity field K-band Imager (HAWK-I) $K_{\rm S}$-band data into account. We take the $K_{\rm S}$-band flux values for 456, 578 and 583 from the HAWK-I UDS and GOODS Survey (HUGS) catalogue (v1.1; Fontana et al. 2014) and rerun EAZY. Our results are illustrated in Figs 13 and 14. The photometric redshift value for 456 remains at $10.91^{-0.92}_{+8.39}$ ($\chi^2 \sim 0$). However, the $z_{\rm phot}$ value seems highly dependent on the J-band upper limit. We thus redetermine the J-band sensitivity limit by measuring the background flux within 35 apertures which are scattered across the CANDELS field. We determine a flux limit close to the value reported by Grogin et al. (2011, measured: 2.62×10^{-2}μJy, reported: 1.97×10^{-2}μJy for a 0.5 arcsec radius aperture). We rerun EAZY and find a value almost identical to the previous result ($z_{\rm phot} = 10.91^{-1.14}_{-7.11}$, $\chi^2 = 0.01$). 456 thus remains a source with a high photometric redshift. The 2σ error bar, computed through the $\Delta\chi^2$ method, does however allow for a low-redshift solution at $z \sim 4$. For 578 the $K_{\rm S}$ band causes the photometric redshift to increase from 6.77 to $7.49^{+0.54}_{-4.60}$ ($\chi^2 = 0.08$). Nonetheless, similar to 456, 578's 2σ error bar permits a $z \sim 3$ solution. For 583, we determine $z_{\rm phot} = 2.68^{+5.61}_{+0.37}$ ($\chi^2 = 0.21$) by including the HUDF deep Y-band and the HUGS K_S-band flux values. This $z_{\rm phot}$ value matches what has previously been reported by Szokoly et al. (2004) for the galaxy next to 583(53.1833, -27.7764). We thus suspect, that 583 might be part of a large clumpy galaxy at low redshift (Schawinski et al. 2011). With the X-ray emission

Table 3. Overview showing all five redshift test results. Sources for which the test indicates $z < 5$ are marked with $\times$. If the redshift test results in $z \geq 5$, we show a. Objects that could not be classified via colour criteria, stacking or the HR are marked with 0. For the HR, we can only distinguish between $z < 4.3$ (HR > 0) and $z \geq 4.3$ (HR ≤ 0). Hence, for the HR means $z \geq 4.3$. After combining all redshift tests, we are left with three possible candidates (arrows). See Table 4 and Table A4 for a detailed overview of the results and the X-ray counts of each individual source.

	ID	Visual classification	Colour criteria	Stacking	HR	Photo-z
	121	×	0	×	×	×
	150	×	0	×	×	×
	173	×	0	×	√	×
	184	×	0	×	×	×
	189	×	0	×	×	×
	199	√	0	√	√	×
	211	×	0	×	×	×
	217	√	0	√	√	×
	221	×	0	×	×	×
	226	×	√	×	×	√
	242	×	0	×	×	×
	244	√	√	√	×	×
	258	√	0	√	×	×
	273	√	0	√	×	×
	296	√	√	√	×	×
	301	×	0	×	×	×
	302	×	0	×	×	×
	303	√	√	0	×	×
	306	√	0	√	×	×
	318	×	0	×	×	×
	321	×	√	×	×	×
	325	×	0	×	×	×
	328	×	0	×	×	×
	331	×	0	×	×	×
	348	√	0	√	×	×
	354	√	0	√	√	×
	371	√	0	√	×	√
	373	×	×	×	×	×
	389	×	0	×	×	×
	392	√	0	√	×	×
	402	√	0	√	×	×
	403	×	0	×	×	×
	410	×	0	×	×	×
	428	×	0	×	×	×
	430	√	0	√	×	√
	444	×	×	×	×	×
	455	×	0	×	×	×
→	456	√	0	√	√	√
	460	√	0	√	√	×
	462	×	0	×	×	×
	466	×	0	×	×	×
	485	√	0	√	×	×
	496	×	0	×	0	×
	522	×	√	√	√	×
	535	×	0	×	√	×
	539	×	0	×	×	×
	546	×	0	×	×	×
	556	×	0	×	×	×
	574	√	0	√	×	×
→	578	√	0	√	0	√
→	583	√	0	√	√	√
	589	×	√	×	×	×
	591	×	0	×	×	×
	620	×	0	×	√	×
	624	√	0	√	×	×
	625	×	0	×	×	×
	630	√	0	×	×	×
	651	√	0	0	×	×

Table 4. Overview over the redshift estimates that we gained for each object in the course of this analysis. All photometric redshifts were gained by using GOODS/ACS, CANDELS and in some cases also *Spitzer* data (marked with an asterisk). For our three final candidates (456, 578, 583), we also computed photometric redshifts using HUDF and HUGS data. Please see Sections 4.3 and 4.4 for the corresponding values. Note that the stacking procedure only gives a redshift indication. Hence, if '4' is given as the stacking result this corresponds to $z \lesssim 4$, '7' indicates $z \gtrsim 7$. We mark sources for which we only gained upper or lower limits on the HR with '*u*' and '*l*'. '0' indicates that a source could not be classified by the corresponding redshift test.

	ID	RA (*Chandra*)	Dec. (*Chandra*)	RA_H	$Dec._H$	Visual	Stacking	Colour criteria	Hardness Ratio (HR)	σ_{HR}	z_{phot}	$\sigma_{phot,+}$	$\sigma_{phot,-}$	χ^2
*	121	53.0268	−27.7653	53.0267	−27.7653	4	4	0	0.21^l	–	1.26	0.64	0.04	14.31
*	150	53.0400	−27.7985	53.0398	−27.7985	4	4	0	0.25^l	–	3.63	0.14	0.16	1.66
	173	53.0477	−27.8351	53.0477	−27.8351	4	4	0	−0.37	0.13	1.28	0.30	0.03	4.11
*	184	53.0523	−27.7748	53.0522	−27.7747	4	4	0	0.19	0.28	1.73	0.05	0.05	2.19
*	189	53.0546	−27.7931	53.0544	−27.7931	4	4	0	0.31^l	–	1.57	0.17	0.07	9.34
*	199	53.0579	−27.8336	53.0579	−27.8336	6	7	0	−0.09	0.10	2.65	0.11	0.08	16.61
	211	53.0620	−27.8511	53.0625	−27.8508	4	4	0	0.06	0.06	1.38	0.29	0.07	11.58
*	217	53.0639	−27.8438	53.0638	−27.8433	0	7	0	−0.17	0.12	3.72	0.40	0.23	38.86
	221	53.0657	−27.8790	53.0660	−27.8787	4	4	0	0.12^l	–	2.05	0.09	0.06	8.84
	226	53.0668	−27.8166	53.0668	−27.8165	4	4	6	0.33^u	–	5.43	0.08	0.12	0.64
*	242	53.0716	−27.7699	53.0713	−27.7696	4	4	0	0.16	0.26	1.60	0.06	0.04	16.75
*	244	53.0721	−27.8190	53.0717	−27.8187	6	7	6	0.29^u	–	1.90	4.32	0.22	2.15
	258	53.0766	−27.8641	53.0766	−27.8644	6	6	0	0.09^l	–	4.22	0.62	3.26	12.49
*	273	53.0821	−27.7673	53.0826	−27.7681	6	7	0	0.03^u	–	3.45	0.20	0.83	1.01
	296	53.0907	−27.7825	53.0913	−27.7820	6	7	6	0.56^l	–	1.99	0.10	0.09	12.71
	301	53.0924	−27.8033	53.0918	−27.8028	4	4	0	0.34	0.10	2.02	0.30	0.29	6.78
*	302	53.0924	−27.8268	53.0923	−27.8260	4	4	0	0.04^u	–	1.05	0.75	0.05	26.22
	303	53.0925	−27.8771	53.0921	−27.8767	5	0	5	0.35^l	–	0.73	3.57	−0.07	0.37
	306	53.0939	−27.8258	53.0944	−27.8259	7	7	0	0.16	0.36	2.87	0.41	0.11	12.30
*	318	53.0965	−27.7449	53.0966	−27.7447	4	4	0	0.38^u	–	1.38	0.06	0.05	34.03
*	321	53.0984	−27.7671	53.0983	−27.7667	4	4	5	0.31^l	–	1.22	0.05	0.03	18.91
	325	53.1000	−27.8086	53.0995	−27.8085	4	4	0	0.46^u	–	2.83	0.23	0.55	7.27
	328	53.1016	−27.8217	53.1012	−27.8224	4	4	0	0.24^u	–	1.68	0.71	1.06	6.38
	331	53.1027	−27.8606	53.1028	−27.8610	4	4	0	0.21^u	–	4.32	0.02	3.63	3.33
*	348	53.1052	−27.8752	53.1058	−27.8753	6	6	0	0.15^u	–	3.11	0.12	0.67	3.85
*	354	53.1076	−27.8558	53.1079	−27.8558	7	7	0	−0.54	0.15	2.83	3.58	0.85	0.38
	371	53.1116	−27.7679	53.1118	−27.7680	5	5	0	0.15	0.10	5.56	0.04	4.50	0.61
	373	53.1118	−27.9096	53.1113	−27.9094	4	4	4	0.22^u	–	2.54	0.15	0.25	12.99
*	389	53.1193	−27.7659	53.1186	−27.7658	4	4	0	0.16^u	–	2.02	0.05	0.48	7.31
*	392	53.1199	−27.7432	53.1198	−27.7436	7	5	0	0.05^u	–	3.07	3.10	0.00	1.31
*	402	53.1219	−27.7529	53.1214	−27.7531	5	5	0	0.27^l	–	2.37	0.64	0.21	2.91
	403	53.1220	−27.9388	53.1224	−27.9381	4	4	0	0.20^l	–	4.22	0.17	0.12	6.97
	410	53.1241	−27.8913	53.1242	−27.8917	4	4	0	0.54	0.12	3.49	0.27	0.27	2.63
*	428	53.1296	−27.8278	53.1295	−27.8276	4	4	0	0.24^u	–	1.15	0.07	0.04	17.71
	430	53.1305	−27.7912	53.1310	−27.7911	0	7	0	0.29	0.15	6.54	1.34	5.07	0.03
*	444	53.1340	−27.7811	53.1340	−27.7809	4	4	4	0.28	0.07	1.42	0.10	0.06	41.98
*	455	53.1378	−27.8022	53.1378	−27.8021	4	4	0	0.21^u	–	1.26	0.05	0.03	5.63
	456	53.1380	−27.8683	53.1381	−27.8684	7	7	0	−0.29	0.11	10.91	−0.92	8.39	0.00
*	460	53.1393	−27.8745	53.1394	−27.8746	0	5	0	−0.02	0.27	2.91	2.68	0.09	0.73
*	462	53.1403	−27.7976	53.1405	−27.7973	4	4	0	0.06	0.39	1.63	0.06	0.04	5.12
	466	53.1417	−27.8167	53.1416	−27.8166	4	4	0	0.27	0.13	2.02	0.20	0.31	5.73
*	485	53.1466	−27.8710	53.1460	−27.8711	7	7	0	0.45	0.15	2.83	0.54	0.68	14.74
	496	53.1505	−27.8890	53.1507	−27.8886	4	4	0	0.00	–	2.50	0.31	2.11	1.44
*	522	53.1585	−27.7741	53.1583	−27.7738	4	5	6	−0.40	0.04	1.60	0.21	0.05	4.06
	535	53.1627	−27.7443	53.1622	−27.7442	4	4	0	−0.12	0.06	2.37	0.30	0.39	3.44
*	539	53.1632	−27.8091	53.1621	−27.8097	4	4	0	0.53^l	–	0.97	0.06	0.08	44.03
	546	53.1653	−27.8142	53.1648	−27.8144	4	4	0	0.29	0.03	3.15	0.18	0.25	8.09
	556	53.1701	−27.9298	53.1699	−27.9304	4	4	0	0.40	0.03	2.68	0.17	0.16	12.11
*	574	53.1787	−27.8027	53.1782	−27.8027	6	7	0	0.38	0.25	3.32	0.42	0.75	2.72
	578	53.1806	−27.7797	53.1807	−27.7796	7	7	0	0.00	–	6.77	0.97	5.10	0.00
	583	53.1835	−27.7766	53.1834	−27.7764	7	7	0	−0.51	0.06	9.36	0.63	4.82	0.00
	589	53.1850	−27.8198	53.1851	−27.8196	4	4	6	0.17^u	–	1.28	0.26	0.08	5.77
*	591	53.1852	−27.7174	53.1848	−27.7173	4	4	0	0.29^u	–	1.35	0.17	0.21	21.54
	620	53.1960	−27.8927	53.1957	−27.8928	4	4	0	−0.02	0.06	2.57	0.55	0.45	4.34
	624	53.1981	−27.8323	53.1979	−27.8319	5	6	0	0.33^l	–	1.52	2.23	0.07	0.56
*	625	53.1989	−27.8440	53.1989	−27.8439	4	4	0	0.71	0.10	1.68	0.07	0.04	16.22
*	630	53.2016	−27.8443	53.2027	−27.8448	7	4	0	0.36^u	–	2.05	5.04	0.16	0.37
*	651	53.2153	−27.8703	53.2150	−27.8695	7	0	0	0.40	0.10	1.90	0.41	0.34	16.22

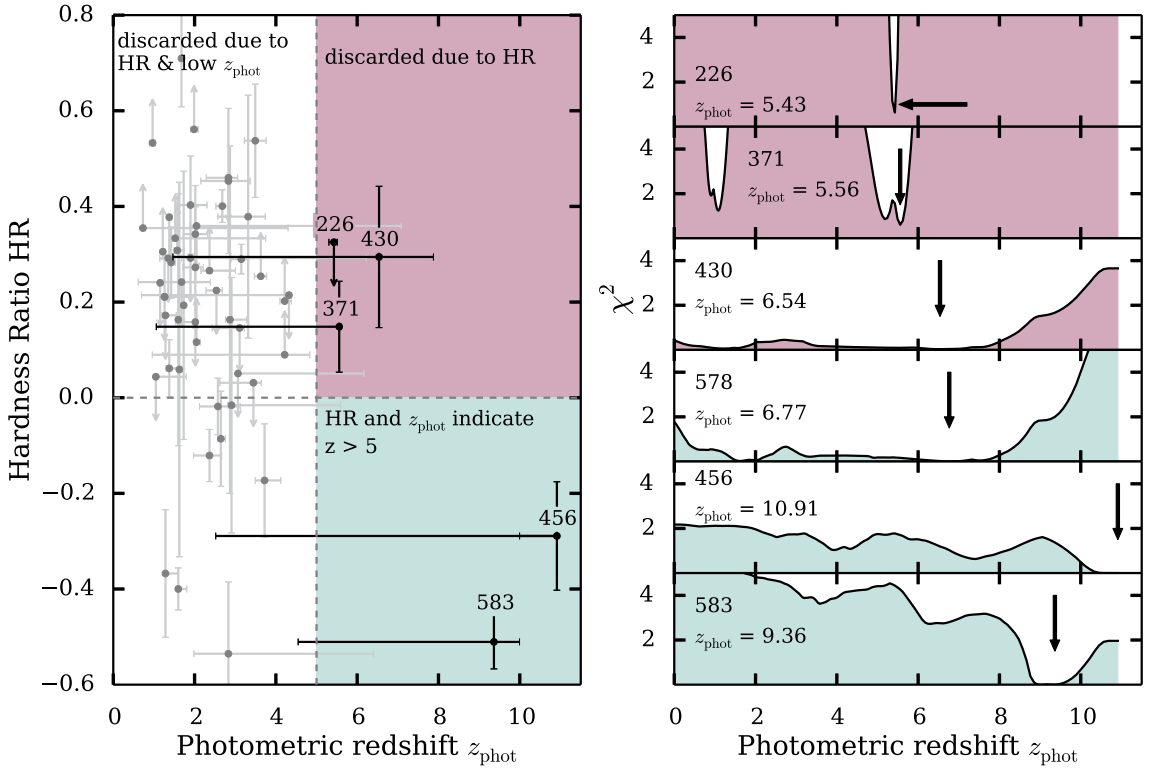

Figure 11. After we combine our visual classifications with our z_{phot}, stacking and colour criteria results, we are left with seven possible candidates. We show their HR and photometric redshift values in the left-hand panel. The right-hand figure illustrates their z_{phot} χ^2 distributions. By also eliminating objects with HR > 0, we are left with three final candidates (456, 578, 583). The left-hand panel does not show sources 496 and 578. These two objects are only detected in the full band and can therefore not be constrained by the HR. While we find a low z_{phot} for 496, 578 has $z_{phot} = 6.77$ and is therefore one of our final high-z candidates. We show 1σ error bars. For the X-ray counts and signal-to-noise ratios of each individual source see Table A4.

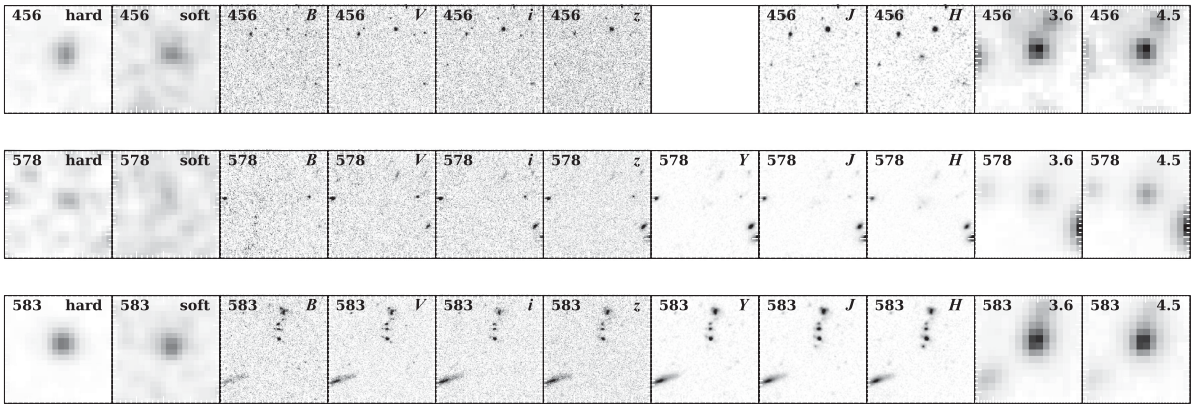

Figure 12. Candidate $z > 5$ AGN that remain after combining all redshift tests. 456, 578 and 583 are the only sources that remain after we combine our stacking ($z_{stacking} \sim 7$ for all), colour criteria (all not classified), HR (456: HR $= -0.289$, 578: not classified, 583: HR $= -0.511$) and photometric redshift code results (456: $z_{phot} = 10.913$, 578: $z_{phot} = 6.766$, 583: $z_{phot} = 9.364$). Visually we classify 456, 578 and 583 as z dropouts. Due to source confusion, we do not use the *Spitzer* 3.6 and 4.5 micron images when running the photometric redshift code for these objects. All images are colour inverted and are 10 arcsec $\times$ 10 arcsec in size.

being offset from what could be the main galaxy, this does remain a very interesting object.

In summary, the HUGS K_S band and HUDF Y band data causes the photometric redshifts of our three final candidates to either drop to low redshift or to allow for a low-redshift solution within a 2σ error bar. Considering these photometric redshift code results and how rare objects as bright as our candidates should be at high redshift, we conclude that 456, 578 and 583 are unlikely to be at high redshift. They do however remain compelling candidates for follow-up observations. 456 remains a very interesting candidate since the 1σ z_{phot} error bar does not allow for lower redshift solutions. 578 could still be at high redshift and 583 is intriguing since the X-ray emission seems to be offset from the main galaxy.

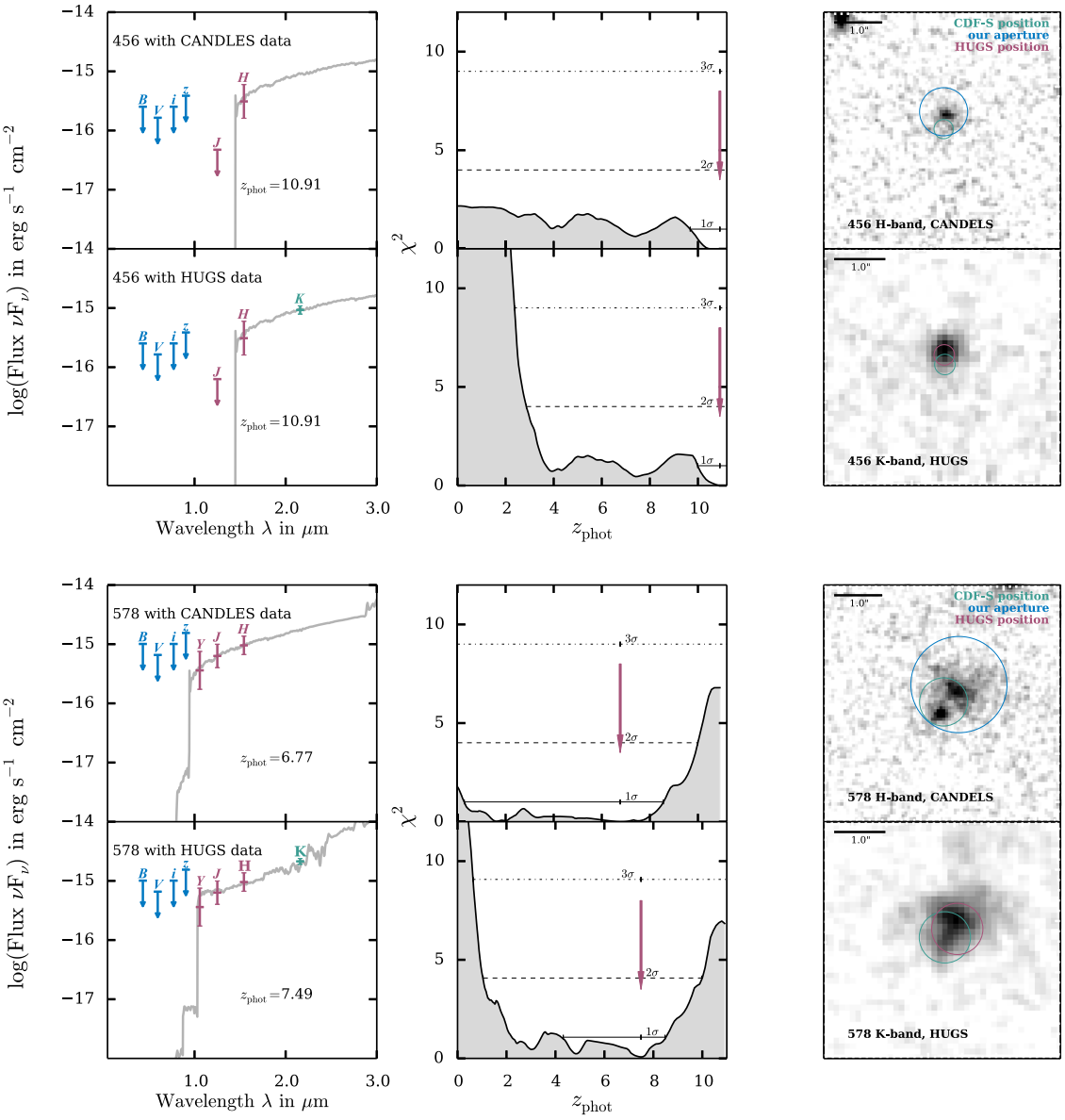

Figure 13. Photometric redshift code results for objects 456 and 578 before (top panels) and after including the HUGS K_S band (bottom panels). After combining all of our redshift tests, we are left with three final candidates (for 583 see Fig. 14). For these we include the HUGS (Fontana et al. 2014) K_S-band values when determining the photometric redshift. We show the best-fitting template SEDs (left), the χ^2 distributions (middle) and the corresponding images (right), before and after including the K_S band. For 456, we redetermine the *J*-band upper limit. Our result is close to the value reported by Grogin et al. (2011) and does not change the $z_{\rm phot}$ result significantly. For both, 456 and 578, a low-redshift solution is allowed within the 2σ error. These two final candidates are hence likely to be at low redshift. We use the $\Delta\chi^2$ method under the assumption of one free parameter ($z_{\rm phot}$) to compute the 1σ, 2σ and 3σ error bars that are shown in the middle panels. All images are colour inverted and are 5 arcsec × 5 arcsec in size.

5 DISCUSSION

5.1 Sensitivity and AGN number density

In this section, we show that our analysis should have been sensitive enough to detect an active BH in a typical high-redshift Lyman Break Galaxy and why we expected to find at least some high z AGN. Furthermore, we determine an upper limit on the AGN number density.

In first step, we determine the BH masses and accretion rates we are sensitive to by calculating the expected X-ray flux as a function of BH mass, Eddington ratio and redshift. We calculate the X-ray luminosity and translate it to observed flux. We use Eddington ratios between 0.01 and 1, and a redshift range from $z = 4$ to $z = 10$. For simplicity, we assume a constant bolometric correction of $k_{\rm corr} = 25$ ($L_{\rm bol} = k_{\rm corr} L_{\rm X}$; Vasudevan & Fabian 2009) and $N_{\rm H} = 10^{22}$ cm^{-2}. Fig. 15 illustrates our results. We also show the *Chandra* 4-Ms flux limits which lie at 9.1×10^{-18} erg s^{-1} cm^{-2} for the soft band and at 5.5×10^{-17} erg s^{-1} cm^{-2} for the hard band (Xue et al. 2011). At $z \sim 5$, we are sensitive to luminosities as low as $\sim 10^{42}$ erg s^{-1} in the soft band and $\sim 10^{43}$ erg s^{-1} in the hard band.

In the GOODS field, the typical stellar mass of a Lyman Break Galaxy at $z \sim 5$ is 2.82×10^{10} M$_\odot$ (Lee et al. 2012). If we use the local BH-stellar mass relation ($M_{\star,\,\rm total}/\ M_{\rm BH} = 562$; Jahnke

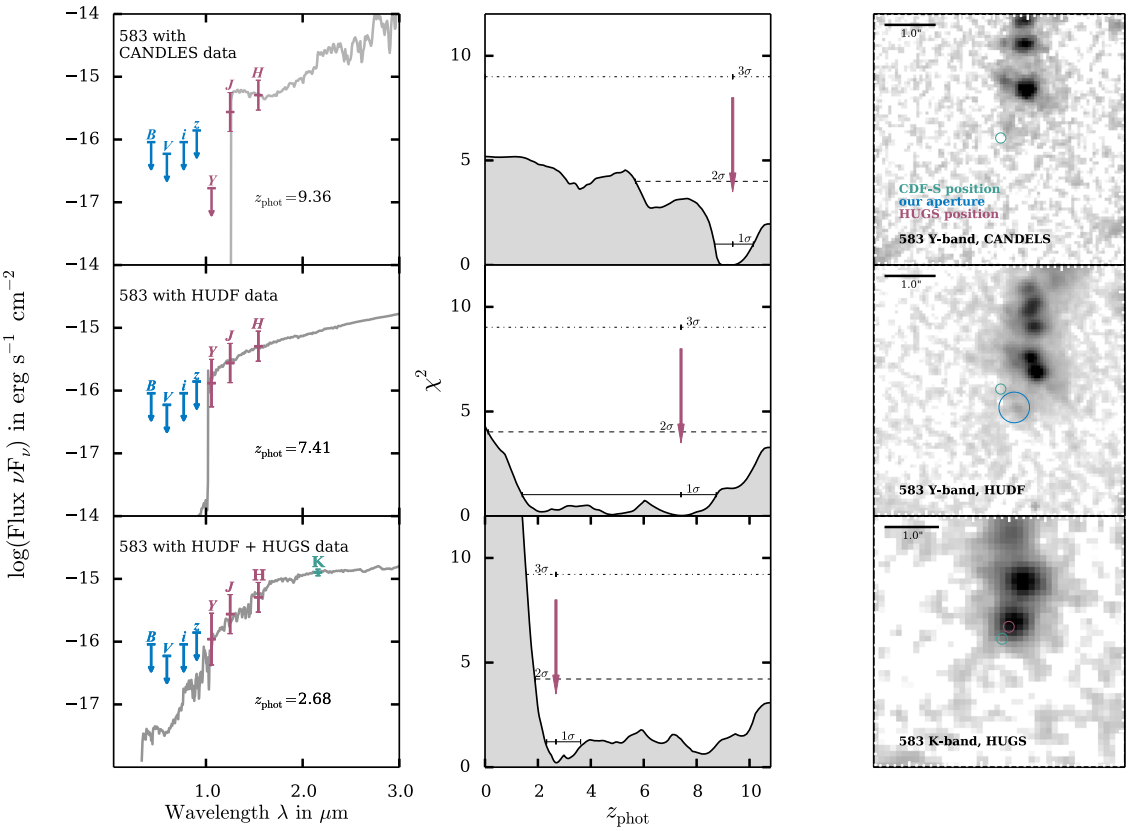

Figure 14. Photometric redshift code results for object 583 before (top panels) and after including the HUDF *Y* band (middle panels) and the HUGS K_S band (bottom panels), analogue to Fig. 13. After combining all of our redshift tests, we are left with three final candidates (for 456 and 578 see Fig. 13). Fortunately, 583 is covered by the HUDF. We thus perform aperture photometry on the deep *HST*/WFC3 HUDF *Y* band and replace the CANDELS *Y*-band value with this flux (middle panels). We also include the HUGS (Fontana et al. 2014) K_S-band value when determining the photometric redshift (bottom row). With the HUDF *Y* band and the HUGS K_S-band 583's photometric redshift value drops to 2.68. It is hence most likely a low-redshift source. We show the best-fitting template SEDs (left), the χ^2 distributions (middle) and the corresponding images (*right*). We use the $\Delta\chi^2$ method under the assumption of one free parameter (z_{phot}) to compute the shown 1σ, 2σ and 3σ error bars. All images are colour inverted and are 5 arcsec × 5 arcsec in size.

et al. 2009) to determine the corresponding BH mass, we find $M_{BH} = 5 \times 10^7\,M_\odot$. Fig. 15 shows that, assuming low obscuration and Eddington ratios >0.1, we should have been capable of detecting such AGN at $z > 5$.

To estimate the number of high z AGN in the CDF-S, we use the results by Bouwens et al. (2014). They find 680 $z \sim 5$, 252 $z \sim 6$ and 113 $z \sim 7$ Lyman Break Galaxies in the CANDELS/Deep and CANDELS/Wide surveys for the GOODS-S field. Nandra et al. (2002) report an AGN fraction of 3 per cent for $z \sim 3$ Lyman Break Galaxies in the *Hubble Deep Field*-North. Assuming that this fraction does not evolve with redshift, we would expect the volume we looked at to contain ∼20 AGN at $z \sim 5$, ∼8 at $z \sim 6$ and ∼3 at $z \sim 7$. Since we are sensitive enough to detect Compton-thin AGN in typical Lyman Break Galaxies, we would have expected to find at least some convincing high-redshift sources. Even if all of our three final candidates (456, 578, 583) would prove to be at high-redshift, the number of high-redshift AGN in our field would still be lower than expected.

We use the estimated number of high redshift AGN to determine an upper limit on the AGN number density. The combined CANDELS/Wide and CANDELS/Deep survey covers an area of 0.03 deg^2. At $z \sim 5$, the faint X-ray selected AGN number density is hence fewer than 655 AGN per deg^2. At $z \sim 6$ and $z \sim 7$, we would expect to find fewer than 262 and 98 AGN per deg^2, respectively. Here, we assumed the $z \sim 3$ Lyman Break Galaxy AGN fraction by Nandra et al. (2002). This AGN fraction could however be especially low for high-redshift Lyman Break Galaxies or generally evolve with redshift. We discuss this in more detail in Section 5.4.

5.2 Comparison to existing work

We compare our results to Vito et al. (2013). They found three $z > 5$ AGN (139, 197, 485) in the CDF-S. Source 139 has a photometric redshift of $z_{phot} = 5.73$ based on Luo et al. (2010). Since 139 is not covered by *B*, *Y*, *J* and *H*, it was not part of our analysis. Object 197 has $z_{phot} = 6.07$ with a secondary solution at $z_{phot} = 4.39$ (Luo et al. 2010). 197 is not in the GOODS field and was therefore immediately excluded by us. Source 485 has a photometric redshift of $z_{phot} = 7.62$ with a secondary solution at $z_{phot} = 3.31$ based on Luo et al. (2010) and has $z_{phot} = 4.42$ according to Santini et al. (2009). Both, Luo et al. (2010) and Santini et al. (2009), did not take CANDELS WFC3/IR data into account when determining photometric redshifts. Instead they used the GOODS - MUSIC catalogue (Grazian et al. 2006) which contains the VLT/ISAAC *J*, *H*, and *K* bands. Taking CANDELS and *Spitzer* data into account, we determined $z_{phot} = 2.83^{+0.54}_{-0.68}$ for object 485.

Vito et al. (2013) also report spectroscopic and photometric redshifts for 31 additional AGN at lower redshifts. Seven of these 31 sources are also part of our sample. For three objects, our photometric redshifts lie within 1σ from the redshift reported

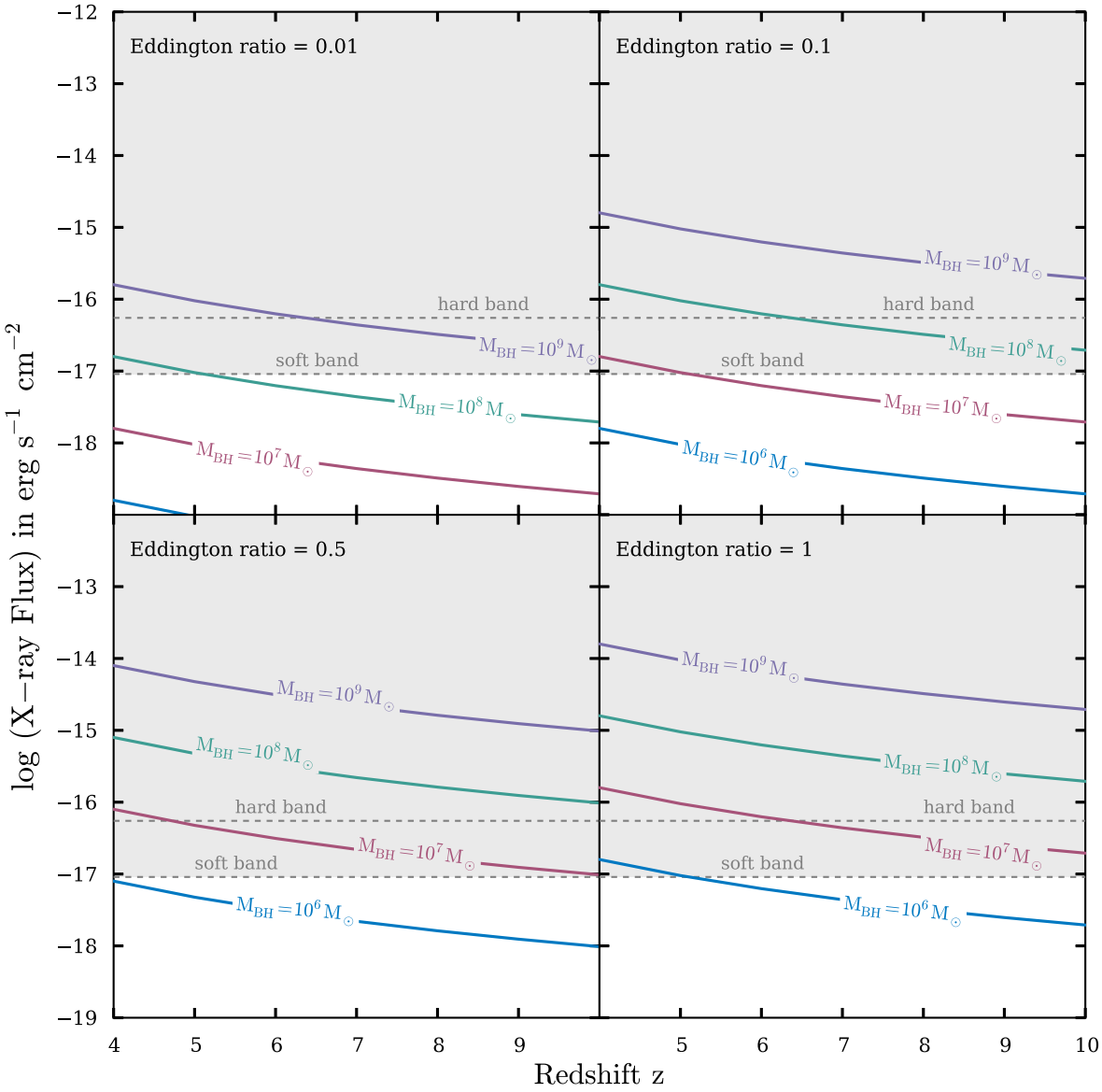

Figure 15. Expected X-ray flux as a function of BH mass, Eddington ratio and redshift. We assume spherical accretion, $N_{\rm H}$ =10^{22} cm^{-2} and a bolometric correction of $k_{\rm corr} = 25$ to calculate the expected X-ray flux for BH masses ranging from 10^6 to 10^9 M$_\odot$, Eddington ratios between 0.01 and 1, and redshifts between $z = 4$ and $z = 10$. The dashed lines show the *Chandra* 4-Ms flux limits in the soft, full and hard bands. The BH mass in a typical Lyman Break Galaxy at $z \sim 5$ is $\sim 10^7$ M$_\odot$. This figure illustrates that we are sensitive enough to detect such sources if we assume low obscuration and an Eddington ratio > 0.1.

by Vito et al. (2013, 331: $z_{\rm phot,Vito} = 3.780$, $z_{\rm phot} = 4.32^{+0.02}_{-3.63}$; 371: $z_{\rm phot,Vito} = 3.10$, $z_{\rm phot} = 5.56^{+0.04}_{-4.50}$; 546: $z_{\rm spec,Vito} = 3.06$, $z_{\rm phot} = 3.15^{+0.18}_{-0.25}$). For four sources, our photometric redshifts do not lie within 1σ (150: $z_{\rm phot,Vito} = 3.34$, $z_{\rm phot} = 3.63^{+0.14}_{-0.16}$; 403: $z_{\rm spec,Vito} = 4.76$, $z_{\rm phot} = 4.22^{+0.17}_{-0.12}$; 556: $z_{\rm phot,Vito} = 3.53$, $z_{\rm phot} = 2.68^{+0.17}_{-0.16}$; 651: $z_{\rm phot,Vito} = 4.66$, $z_{\rm phot} = 1.90^{+0.41}_{-0.34}$). The remaining 24 low-redshift AGN were not part of our sample because they were not covered by enough bands (*B*, *V*, *i*, *z*, *J*, *H*), because they were clearly visible in all bands and therefore discarded as $z < 5$ sources or because their images were disturbed by artefacts. Except for source 485 and the four low-redshift AGN (150, 403, 556, 651) our findings do hence agree with the results by Vito et al. (2013).

Treister et al. (2013) searched for X-ray emission of $z = 6$–8 Lyman Break dropout and photometrically selected sources. None of the ∼600 $z \sim 6$, ∼150 $z \sim 7$ or ∼80 $z \sim 8$ sources could be detected individually in the X-rays. Stacking the X-ray data in redshift bins did not generate a significant detection either. In the stacks, the 3σ upper limits on the X-ray emission lay at $\sim 10^{41}$ erg s^{-1} (soft) and $\sim 10^{42}$ erg s^{-1} (hard) for the $z \sim 6$ and $z \sim 7$ bins. Assuming a bolometric correction of $k_{\rm corr} = 25$ (Vasudevan & Fabian 2009) and an Eddington ratio of 0.1, these upper limits correspond to $\sim 10^5$ M$_\odot$ (soft) and $\sim 10^6$ M$_\odot$ (hard) in terms of BH mass. In comparison to our work, Treister et al. (2013) based their search on a sample of optically selected sources, whereas we selected our objects in the X-rays. Nonetheless, the results are in agreement.

5.3 $z \gtrsim 5$ AGN in the CDF-S

In this work, we searched for possible $z > 5$ AGN candidates in the CDF-S. In contrast to Treister et al. (2013), we started out with a sample of confirmed X-ray sources. We used visual classification,

colour criteria, stacking, a photometric redshift code and the HR to obtain multiple redshift indications. After dismissing sources for which our redshift tests indicated $z < 5$, three final candidates with $z_{\rm phot} \sim 7$ (578), $z_{\rm phot} \sim 9$ (583) and $z_{\rm phot} \sim 10$ (456) remained in our sample. Our comparison to the galaxy luminosity function showed that $z \sim 7$, $z \sim 9$ and $z \sim 10$ objects as bright as 578, 583 and 456 are rare. By including the HUGS K_S band (Fontana et al. 2014) and the HUDF Y-band data, the photometric redshifts for our three final candidates either dropped to low-redshift (583) or allowed for a low-redshift solution within 2σ error bars (578, 583). Our three final candidates did hence not pass this extended redshift test. We conclude that considering our photometric redshift code results and the rarity of such high-redshift objects, 456, 578 and 583 are most likely low-redshift sources. We also found five low-significance objects. These sources are detected in the X-rays, but they do not seem to possess a counterpart in the optical or infrared (including the *Spitzer*/IRAC 3.6 and 4.5 micron channels and the VLT/HAWK-I K_S band). The currently available data does not allow us to constrain their redshifts or determine if these objects are spurious detections.

Based upon currently available GOODS/ACS, CANDELS and *Spitzer* data, the analysis did therefore yield three final $z > 5$ candidates and five low-significance objects for this deep, but narrow field. Including HUGS and HUDF data did however show, that 456, 578 and 583 are likely to be at low redshift. Follow-up observations are necessary to gain more reliable redshifts for our three final candidates and to constrain the nature of our five low-significance objects.

5.4 Possible explanations

Both, the approach by Treister et al. (2013) and our approach, assumed that X-ray emission is a valid tracer for BH growth. If at high redshift, BHs primarily grow through BH mergers instead of accretion, electromagnetic radiation might not be emitted during the growth process. X-ray emission might hence not be an indicator for active BHs.

At high redshift, the number of actively accreting BHs could also be generally low. This could be caused by a low BH occupation fraction, a low AGN fraction or BH growth through short, super-Eddington episodes. We stress the difference between the BH occupation fraction and the AGN fraction since they describe different scenarios.

If the BH occupation fraction is low only very few haloes are seeded with BHs. Our sample could therefore be too small to not only contain a BH, but to contain a BH that is also actively accreting.

Even if the BH occupation fraction is high, the AGN fraction could still be low. So, even if there are plenty of BHs in our field, only few of them could be active. For instance, BHs at high redshift could only grow in optically faint galaxies. In our analysis, these faint galaxies could correspond to the low-significance objects that do not seem to possess an optical or infrared counterpart (190, 280, 333, 384, 643, see Section 3.3). The currently available data does not allow us to investigate these sources further. We are however hopeful that the forthcoming 7-Ms survey for the CDF-S (PI: William Brandt, Proposal ID: 15900132) will show if these objects are real.

BHs could also grow through short, super-Eddington accretion phases (Madau et al. 2014; Volonteri & Silk 2014). Madau et al. (2014) illustrated that a duty cycle of 20 per cent is enough to grow a $100\,{\rm M}_\odot$ non-rotating seed BH into a $\sim 10^9\,{\rm M}_\odot$ BH by $z \sim 7$. This could, for instance, be realized through five 20 Myr long growth episodes with $\dot{m}/\dot{m}_{\rm Edd} = 4$, each followed by a 100 Myr phase of quiescence. The Treister et al. (2013) and our sample, could thus not contain any BHs that are actively accreting at the time of observation.

Simulations suggest that the BH occupation fraction should be high enough for our field to contain high-redshift BHs. Menou, Haiman & Narayanan (2001) ran Monte Carlo simulations of the merger history of dark matter haloes. They showed that to reproduce the local BH distribution, >3 per cent of the $M_{\rm halo} \gtrsim 10^8\,{\rm M}_\odot$ haloes should be seeded with BHs at $z \sim 5$.

Bellovary et al. (2011) ran smoothed particle hydrodynamics+N-body simulations in which only the local gas properties, such as density, temperature and metallicity, influence the BH formation and evolution. They showed that the BH occupation fraction is halo mass dependent. At $z \sim 5$, they found a BH occupation fraction of $\sim$50 per cent for $10^8\,{\rm M}_\odot < M_{\rm halo} < 10^9\,{\rm M}_\odot$ haloes and a fraction of 100 per cent for $M_{\rm halo} > 10^9\,{\rm M}_\odot$ haloes.

Alexander & Natarajan (2014) presented a sophisticated model in which a BH seed is being fed by dense cold gas flows while it is embedded in a nuclear star cluster. This can lead to supraexponential accretion and could explain how a light ($\sim 10\,{\rm M}_\odot$) Pop III remnant BH seed could grow into a $\gtrsim 10^4\,{\rm M}_\odot$ seed within $\sim 10^7$ yr. Nevertheless, these $\gtrsim 10^4\,{\rm M}_\odot$ seeds still need to grow into the massive $10^9\,{\rm M}_\odot$ sources that we find at $z > 6$. This most likely happens via Eddington limited accretion. The distribution of high-redshift quasars that we observe at $z > 6$ can be reproduced if the supraexponential accretion and the subsequent Eddington-limited growth work efficiently in at least 1–5 per cent of the dark matter haloes.

Stark et al. (2009), Vanzella et al. (2009), Wilkins et al. (2010), Bouwens et al. (2014), Duncan et al. (2014) and many more have shown that the GOODS-south field contains hundreds of $z \gtrsim 5$ Lyman Break Galaxies. These high-redshift sources should have passed our manual inspection, the colour criteria, the stacking and the photometric redshift measurement. So, according to the simulations and the number of high-redshift Lyman Break Galaxies in our field, we would expect our sample to include high-redshift BHs. The number of actively accreting BHs could however still be low. For instance, it would be possible that only the most massive haloes host AGN.

Finding one or more high-redshift AGN would have opened up the window to the early BH growth era. Treister et al. (2011) showed that the massive and luminous quasars we observe at $z > 6$ are most likely not representative of the entire high-redshift BH population. Such quasars are rare and presumably only constitute the high-mass end of the entire BH population (Volonteri 2010). At $z \sim 6$, we expect to find only $\sim$2 in a 1000 deg^2 field (Fan et al. 2000, 2001). Furthermore, these objects only allow us limited insight into seed formation scenarios. For typical seed masses $\lesssim 10^6\,{\rm M}_\odot$, these objects have to undergo multiple Salpeter times (Salpeter 1964) to reach $M_{\rm BH} \sim 10^9\,{\rm M}_\odot$. By the time we observe them as quasars, all initial seed information will be lost. We are hence especially interested in the population of more abundant, less massive, less luminous AGN that will end up in galaxies similar to the Milky Way. If our analysis had yielded a convincing high-redshift AGN candidate, we would have been able to put first constraints on this more representative and revealing BH population.

To constrain the explanations for our results and to gain further insights into BH formation and growth at high redshift, this analysis needs to be repeated for a larger sample. Especially constraining the BH occupation fraction and the short, super-Eddington growth scenario requires a larger field. The new field does not need to be deeper, but wider than the 0.11 deg^2 CDF-S (Luo et al. 2008). The

2.8-Ms *Chandra* COSMOS Legacy Survey, for which the data will be available soon, covers a 2.2 deg^2 area (Civano & the Chandra COSMOS Legacy Team 2014). Not being as deep as the 4-Ms *Chandra* data, the *Chandra* COSMOS Legacy Survey will probe a slightly different parameter space (see Treister et al. 2011 for an illustration of the high-redshift number density that is necessary for an individual detection). Nonetheless, it will provide data for a much wider field and will thus enable us to repeat this analysis for a larger sample. The Advanced Telescope for High Energy Astrophysics (ATHENA), which is meant to be launched in 2028, will allow us to constrain the BH occupation fraction to new accuracy. With its X-ray Wide Field Imager, ATHENA is meant to detect over 400 $z = 6$–8 and over 30 $z > 8$ X-ray selected active BHs (Aird et al. 2013; Nandra et al. 2013). James Webb Space Telescope (JWST) data could help to investigate the nature of our five low-significance objects.

6 SUMMARY

We searched for $z \gtrsim 5$ AGN in the CDF-S. We used the *Chandra* 4-Ms catalogue and combined it with GOODS/ACS, CANDELS/WFC3 and *Spitzer*/IRAC data. Our main sample contained 58 sources. We ran a photometric redshift code, stacked the GOODS/ACS data, applied colour criteria and the Lyman Break Technique. Furthermore, we used the X-ray HR as a redshift indicator. After combining all redshift tests, three final $z \gtrsim 5$ AGN candidates remained. Redetermining their photometric redshifts with additional VLT/HAWK-I HUGS K_S band and *HST*/WFC3 HUDF *Y*-band data showed, that they are most likely low-redshift sources. We also found five sources that are detected in the X-rays, but that do not seem to possess a counterpart in the optical or infrared (low-significance objects). The currently available data did not allow us to determine if these objects are possible high-redshift AGN candidates, spurious detections or optically faint low-redshift sources. Assuming that our three final candidates are indeed low-redshift sources and that our five low-significance objects are either spurious detections or also at low redshift, we concluded that the CDF-S does not contain any high-redshift AGN. We also showed that we should have been able to detect active BHs in typical $z \sim 5$ Lyman Break Galaxies and why we would have expected to find at least some high z AGN. Our results could be explained by

(i) a low BH occupation fraction or a low AGN fraction. If at high redshift, only very few haloes contain a BH or only very few BHs are actively accreting, our sample could be too small to contain an AGN.

(ii) BH growth via short, super-Eddington growth modes. If BHs primarily grow through short accretion episodes, the number of actively accreting BHs in our sample might be zero.

(iii) BH growth in optically faint galaxies. Our five low-significance objects could indicate that high-redshift AGN primarily grow in galaxies that we do not detect in the optical. We were however unable to constrain their redshifts and noted that these could be spurious detections.

(iv) BH growth via BH–BH mergers. If at high z, BHs primarily grow through mergers instead of accretion, X-rays might not trace BH growth.

ACKNOWLEDGEMENTS

We thank Andreas Faisst for helpful discussions and Richard Ellis for suggesting the stacking analysis. We also thank the anonymous referee for helpful comments. AKW, KS and MK gratefully acknowledge support from Swiss National Science Foundation Grant PP00P2_138979/1. Support for the work of ET was provided by the Center of Excellence in Astrophysics and Associated Technologies (PFB 06), by the FONDECYT regular grant 1120061 and by the CONICYT Anillo project ACT1101. This research has made use of NASA's ADS Service. This research made use of Astropy, a community-developed core PYTHON package for Astronomy (Astropy Collaboration, 2013). The scientific results reported in this article are based to a significant degree on data obtained from the Chandra Data Archive. This work is based on observations taken by the CANDELS Multi-Cycle Treasury Program with the NASA/ESA HST, which is operated by the Association of Universities for Research in Astronomy, Inc., under NASA contract NAS5-26555. This work is based on observations made with the Spitzer Space Telescope, which is operated by the Jet Propulsion Laboratory, California Institute of Technology under a contract with NASA.

REFERENCES

Aird J. et al., 2013, preprint (arXiv:1306.2325)
Ajello M., 2009, preprint (arXiv:0902.3033)
Alexander T., Natarajan P., 2014, Science, 345, 1330
Alvarez M. A., Wise J. H., Abel T., 2009, ApJ, 701, L133
Arnaud K. A., 1996, in Jacoby G. H., Barnes J., eds, ASP Conf. Ser. Vol. 101, Astronomical Data Analysis Software and Systems V. Astron. Soc. Pac., San Francisco, p. 17
Barth A. J., Martini P., Nelson C. H., Ho L. C., 2003, ApJ, 594, L95
Beckwith S. V. W. et al., 2006, AJ, 132, 1729
Bellovary J., Volonteri M., Governato F., Shen S., Quinn T., Wadsley J., 2011, ApJ, 742, 13
Bertin E., Arnouts S., 1996, A&AS, 117, 393
Bertin E., Mellier Y., Radovich M., Missonnier G., Didelon P., Morin B., 2002, in Bohlender D. A., Durand D., Handley T. H., eds, ASP Conf. Ser. Vol. 281, Astronomical Data Analysis Software and Systems XI. Astron. Soc. Pac., San Francisco, p. 228
Blanton M. R., Roweis S., 2007, AJ, 133, 734
Bouwens R. J. et al., 2014, preprint (arXiv:1403.4295)
Brammer G. B., van Dokkum P. G., Coppi P., 2008, ApJ, 686, 1503
Brightman M., Nandra K., 2012, MNRAS, 422, 1166
Bromm V., Yoshida N., 2011, ARA&A, 49, 373
Bromm V., Coppi P. S., Larson R. B., 2002, ApJ, 564, 23
Bromm V., Yoshida N., Hernquist L., McKee C. F., 2009, Nature, 459, 49
Calzetti D., Armus L., Bohlin R. C., Kinney A. L., Koornneef J., Storchi-Bergmann T., 2000, ApJ, 533, 682
Civano F. M., the Chandra COSMOS Legacy Team 2014, in American Astronomical Society Meeting Abstracts, Vol. 223, First results from the Chandra COSMOS Legacy survey. Am. Astron. Soc., Washington, DC, p. 254.46
Comastri A., Iwasawa K., Gilli R., Vignali C., Ranalli P., Matt G., Fiore F., 2010, ApJ, 717, 787
Dahlen T. et al., 2010, ApJ, 724, 425
Damen M. et al., 2011, ApJ, 727, 1
Duncan K. et al., 2014, MNRAS, 444, 2960
Dunlop J. S., 2013, in Wiklind T., Mobasher B., Bromm V., eds, Astrophysics and Space Science Library, Vol. 396, The First Galaxies, Springer-Verlag, Berlin, p. 223
Dunlop J. S., Cirasuolo M., McLure R. J., 2007, MNRAS, 376, 1054
Fan X. et al., 2000, AJ, 120, 1167
Fan X. et al., 2001, AJ, 122, 2833
Finkelstein S. L. et al., 2012, ApJ, 756, 164
Fiore F. et al., 2009, ApJ, 693, 447
Fontana A. et al., 2014, A&A, 570, A11
Genzel R., Thatte N., Krabbe A., Kroker H., Tacconi-Garman L. E., 1996, ApJ, 472, 153

Ghez A. M., Klein B. L., Morris M., Becklin E. E., 1998, ApJ, 509, 678
Ghez A. M., Morris M., Becklin E. E., Tanner A., Kremenek T., 2000, Nature, 407, 349
Ghez A. M. et al., 2008, ApJ, 689, 1044
Giavalisco M., 2002, ARA&A, 40, 579
Giavalisco M. et al., 2004, ApJ, 600, L93
Grazian A. et al., 2006, A&A, 449, 951
Grogin N. A. et al., 2011, ApJS, 197, 35
Guhathakurta P., Tyson J. A., Majewski S. R., 1990, ApJ, 357, L9
Haiman Z., Loeb A., 2001, ApJ, 552, 459
Holwerda B. W., 2005, preprint (arXiv:astro-ph/0512139)
Illingworth G. D. et al., 2013, ApJS, 209, 6
Jahnke K. et al., 2009, ApJ, 706, L215
Johnson J. L., Whalen D. J., Fryer C. L., Li H., 2012, ApJ, 750, 66
Koekemoer A. M. et al., 2011, ApJS, 197, 36
Koekemoer A. M. et al., 2013, ApJS, 209, 3
Latif M. A., Schleicher D. R. G., Schmidt W., Niemeyer J. C., 2013, MNRAS, 436, 2989
Lee K.-S. et al., 2012, ApJ, 752, 66
Loeb A., Rasio F. A., 1994, ApJ, 432, 52
Luo B. et al., 2008, ApJS, 179, 19
Luo B. et al., 2010, ApJS, 187, 560
Lusso E. et al., 2010, A&A, 512, A34
Madau P., Rees M. J., 2001, ApJ, 551, L27
Madau P., Haardt F., Dotti M., 2014, ApJL, 784, L38
McLure R. J., Dunlop J. S., Cirasuolo M., Koekemoer A. M., Sabbi E., Stark D. P., Targett T. A., Ellis R. S., 2010, MNRAS, 403, 960
McLure R. J. et al., 2011, MNRAS, 418, 2074
Magorrian J. et al., 1998, AJ, 115, 2285
Menou K., Haiman Z., Narayanan V. K., 2001, ApJ, 558, 535
Mortlock D. J. et al., 2011, Nature, 474, 616
Murphy K. D., Yaqoob T., 2009, MNRAS, 397, 1549
Nandra K., Mushotzky R. F., Arnaud K., Steidel C. C., Adelberger K. L., Gardner J. P., Teplitz H. I., Windhorst R. A., 2002, ApJ, 576, 625
Nandra K. et al., 2013, preprint (arXiv:1306.2307)
Oke J. B., Gunn J. E., 1983, ApJ, 266, 713
Rees M. J., Volonteri M., 2007, in Karas V., Matt G., eds, Proc. IAU Symp. 238, Black Holes from Stars to Galaxies – Across the Range of Masses. Cambridge Univ. Press, Cambridge, p. 51
Salpeter E. E., 1964, ApJ, 140, 796
Santini P. et al., 2009, A&A, 504, 751
Schawinski K., Urry M., Treister E., Simmons B., Natarajan P., Glikman E., 2011, ApJ, 743, L37
Schödel R., Ott T., Genzel R., Eckart A., Mouawad N., Alexander T., 2003, ApJ, 596, 1015
Stark D. P., Ellis R. S., Bunker A., Bundy K., Targett T., Benson A., Lacy M., 2009, ApJ, 697, 1493
Steffen A. T., Strateva I., Brandt W. N., Alexander D. M., Koekemoer A. M., Lehmer B. D., Schneider D. P., Vignali C., 2006, AJ, 131, 2826
Steidel C. C., Hamilton D., 1992, AJ, 104, 941
Steidel C. C., Adelberger K. L., Giavalisco M., Dickinson M., Pettini M., 1999, ApJ, 519, 1
Szokoly G. P. et al., 2004, ApJS, 155, 271
Tananbaum H. et al., 1979, ApJ, 234, L9
Tozzi P. et al., 2006, A&A, 451, 457
Trakhtenbrot B., Netzer H., Lira P., Shemmer O., 2011, ApJ, 730, 7
Treister E., Urry C. M., Virani S., 2009, ApJ, 696, 110
Treister E., Schawinski K., Volonteri M., Natarajan P., Gawiser E., 2011, Nature, 474, 356
Treister E., Schawinski K., Volonteri M., Natarajan P., 2013, ApJ, 778, 130
Turner T. J., George I. M., Nandra K., Mushotzky R. F., 1997, ApJS, 113, 23
van Dokkum P. et al., 2005, Spitzer Proposal, 20708
Vanzella E. et al., 2009, ApJ, 695, 1163
Vasudevan R. V., Fabian A. C., 2009, MNRAS, 392, 1124
Vignali C., Brandt W. N., Schneider D. P., 2003, AJ, 125, 433
Vito F. et al., 2013, MNRAS, 428, 354
Volonteri M., 2010, A&AR, 18, 279
Volonteri M., Begelman M. C., 2010, MNRAS, 409, 1022
Volonteri M., Rees M. J., 2005, ApJ, 633, 624
Volonteri M., Silk J., 2014, preprint (arXiv:1401.3513)
Wang J. X., Malhotra S., Rhoads J. E., Norman C. A., 2004, ApJ, 612, L109
Wilkes B. J., Tananbaum H., Worrall D. M., Avni Y., Oey M. S., Flanagan J., 1994, ApJS, 92, 53
Wilkins S. M., Bunker A. J., Ellis R. S., Stark D., Stanway E. R., Chiu K., Lorenzoni S., Jarvis M. J., 2010, MNRAS, 403, 938
Willott C. J., McLure R. J., Jarvis M. J., 2003, ApJ, 587, L15
Xue Y. Q. et al., 2011, ApJS, 195, 10

APPENDIX A: ADDITIONAL FIGURES AND TABLES

Table A1. SExtractor parameter values. We adjusted the aperture size (PHOT_APERTURES) and the minimum number of pixels above the threshold for a detection (DETECT_MINAREA) for each source individually. Table A2 summarizes these values for each of our main sample sources. Note that the values given for PHOT_APERTURES corresponds to the aperture diameter, not radius.

Keyword	Value
CATALOG_TYPE	ASCII_HEAD
DETECT_MINAREA	20–90
DETECT_THRESH	0.5
DEBLEND_NTHRESH	32
DEBLEND_MINCONT	0.001
WEIGHT_TYPE	MAP_VAR
PHOT_APERTURES	0.6-2.0 arcsec
PHOT_AUTOPARAMS	2.5, 3.5
PHOT_PETROPARAMS	2.0, 3.5

Table A2. SExtractor DETECT_MINAREA and PHOT_APERTURES parameter values for each of our main sample sources. Note that the values given for PHOT_APERTURES corresponds to the aperture diameter, not radius.

ID	DETECT_MINAREA	PHOT_APERTURES	ID	DETECT_MINAREA	PHOT_APERTURES
121	20	2.0 arcsec	392	20	2.0 arcsec
150	20	2.0 arcsec	402	20	1.0 arcsec
173	20	1.0 arcsec	403	20	1.0 arcsec
184	40	1.5 arcsec	410	20	1.2 arcsec
189	20	1.0 arcsec	428	20	1.0 arcsec
199	60	2.0 arcsec	430	80	1.5 arcsec
211	50	1.0 arcsec	444	30	1.0 arcsec
217	40	1.5 arcsec	455	20	2.0 arcsec
221	30	1.5 arcsec	456	20	1.0 arcsec
226	20	2.0 arcsec	460	20	2.0 arcsec
242	50	1.5 arcsec	462	20	1.0 arcsec
244	20	2.0 arcsec	466	20	1.5 arcsec
258	20	0.6 arcsec	485	70	2.0 arcsec
273	70	2.0 arcsec	496	20	1.0 arcsec
296	20	1.0 arcsec	522	20	1.0 arcsec
301	30	2.0 arcsec	535	40	1.0 arcsec
302	20	1.0 arcsec	539	30	1.0 arcsec
303	80	2.0 arcsec	546	30	1.0 arcsec
306	90	1.5 arcsec	556	20	2.0 arcsec
318	20	2.0 arcsec	574	20	1.5 arcsec
321	30	2.0 arcsec	578	90	2.0 arcsec
325	20	1.0 arcsec	583	50	0.6 arcsec
328	20	1.5 arcsec	589	50	1.5 arcsec
331	20	1.0 arcsec	591	60	1.0 arcsec
348	20	1.5 arcsec	620	20	2.0 arcsec
354	20	1.5 arcsec	624	20	1.0 arcsec
371	20	1.0 arcsec	625	20	1.5 arcsec
373	50	2.0 arcsec	630	90	2.0 arcsec
389	20	1.0 arcsec	651	90	2.0 arcsec

Table A3. Signal-to-noise ratio statistics. Out of the 740 objects in the *Chandra* 4-Ms catalogue 371 have intact images and are covered by enough filters (*B*, *V*, *i*, *z*, *J*, *H*). We show the number of sources with signal-to-noise ratios ≥1 and ≥5

Number of objects with sufficient filter coverage and intact images: 371	
Out of these 371 sources, number of objects with a signal-to-noise ratio ≥1:	
In the soft band:	324 (87.3 per cent)
In the hard band:	172 (46.4 per cent)
In the full band:	303 (81.7 per cent)
In the hard and the soft band:	139 (37.5 per cent)
In the soft, hard or full band:	371 (100 per cent)
Out of these 371 sources, number of objects with a signal-to-noise ratio ≥5:	
In the soft band:	110 (29.6 per cent)
In the hard band:	96 (25.9 per cent)
In the full band:	134 (36.1 per cent)
In the hard and the soft band:	74 (19.9 per cent)
In the soft, hard or full band:	140 (37.7 per cent)

Table A4. HR values, X-ray counts, errors on the X-ray counts and signal-to-noise ratio values for the main sample. The HR values were calculated using equation (4). Upper and lower limits on the HR are indicated with '*u*' and '*l*', respectively. Objects for which the HR could not be determined due to an upper limit in both the Hard and the Soft band, are marked with '0.00'. The X-ray count values were directly extracted from the Xue et al. (2011) catalogue. For the errors on the X-ray counts, we give the upper errors given in the 4-Ms catalogue. For objects that are not detected, we give an upper limit on the X-ray counts, set σ to −1.00 and mark the signal-to-noise ratio with a dash.

ID	HR	σ_{HR}	Hard counts	σ_{Hard}	SNR_{Hard}	Soft counts	σ_{Soft}	SNR_{Soft}	Full	σ_{Full}	SNR_{Full}
121	0.21^{l}	–	37.15	13.41	2.77	24.21	−1.00	–	53.15	15.51	3.43
150	0.25^{l}	–	30.02	10.54	2.85	17.86	−1.00	–	38.59	11.89	3.25
173	−0.37	0.13	40.17	11.14	3.61	86.87	11.70	7.42	126.81	15.39	8.24
184	0.19	0.28	23.81	9.82	2.42	16.10	6.63	2.43	39.82	11.21	3.55
189	0.31^{l}	–	29.33	9.36	3.13	15.52	−1.00	–	37.01	10.46	3.54
199	−0.09	0.10	80.88	12.71	6.36	96.07	11.95	8.04	176.50	16.78	10.52
211	0.06	0.06	224.79	19.43	11.57	198.79	16.60	11.98	422.57	24.89	16.98
217	−0.17	0.12	58.49	11.84	4.94	82.96	11.29	7.35	141.11	15.65	9.02
221	0.12^{l}	–	28.38	12.27	2.31	22.47	−1.00	–	43.08	14.21	3.03
226	0.33^{u}	–	19.07	−1.00	–	9.71	5.14	1.89	21.36	−1.00	–
242	0.16	0.26	23.04	8.77	2.63	16.58	6.38	2.60	39.52	10.21	3.87
244	0.29^{u}	–	20.66	−1.00	–	11.32	5.27	2.15	22.15	7.56	2.93
258	0.09^{l}	–	22.21	9.43	2.36	18.55	−1.00	–	33.35	11.09	3.01
273	0.03^{u}	–	21.44	−1.00	–	20.14	6.46	3.12	28.12	8.58	3.28
296	0.56^{l}	–	51.01	10.12	5.04	14.34	−1.00	–	59.21	10.98	5.39
301	0.34	0.10	94.01	12.70	7.40	46.08	8.57	5.38	139.58	14.74	9.47
302	0.04^{u}	–	20.23	−1.00	–	18.53	6.17	3.00	26.87	8.06	3.33
303	0.35^{l}	–	35.90	11.17	3.21	17.10	−1.00	–	41.77	12.31	3.39
306	0.16	0.36	13.22	6.87	1.92	9.51	5.09	1.87	22.65	7.91	2.86
318	0.38^{u}	–	26.29	−1.00	–	11.88	6.01	1.98	22.50	9.49	2.37
321	0.31^{l}	–	25.16	8.52	2.95	13.39	−1.00	–	30.41	9.36	3.25
325	0.46^{u}	–	18.65	−1.00	–	6.90	4.43	1.56	15.28	6.48	2.36
328	0.24^{u}	–	14.56	−1.00	–	8.89	4.78	1.86	17.55	−1.00	–
331	0.21^{u}	–	18.00	−1.00	–	11.64	5.59	2.08	21.71	−1.00	–
348	0.15^{u}	–	24.86	−1.00	–	18.53	6.82	2.72	21.72	9.66	2.25
354	−0.54	0.15	21.55	8.50	2.54	71.22	10.41	6.84	92.58	12.69	7.30
371	0.15	0.10	99.88	13.25	7.54	74.06	10.52	7.04	173.34	16.29	10.64
373	0.22^{u}	–	40.47	−1.00	–	25.64	9.80	2.62	46.27	−1.00	–
389	0.16^{u}	–	19.56	−1.00	–	14.22	5.72	2.49	18.45	7.61	2.42
392	0.05^{u}	–	21.97	−1.00	–	19.85	6.95	2.86	27.31	−1.00	–
402	0.27^{l}	–	20.27	8.72	2.32	11.76	−1.00	–	27.82	−1.00	–
403	0.20^{l}	–	56.82	22.53	2.52	37.72	−1.00	–	82.03	25.80	3.18
410	0.54	0.12	99.62	15.79	6.31	29.98	8.78	3.41	129.43	17.59	7.36
428	0.24^{u}	–	16.26	−1.00	–	9.96	4.93	2.02	13.34	6.32	2.11
430	0.29	0.15	50.46	10.11	4.99	27.51	6.99	3.94	77.68	11.68	6.65
444	0.28	0.07	158.67	15.81	10.04	88.73	11.29	7.86	246.58	18.84	13.09
455	0.21^{u}	–	18.58	−1.00	–	12.11	5.26	2.30	20.22	7.02	2.88
456	−0.29	0.11	55.26	11.88	4.65	100.21	12.27	8.17	155.15	16.35	9.49
460	−0.02	0.27	23.19	9.95	2.33	23.93	7.62	3.14	47.01	11.84	3.97
462	0.06	0.39	10.69	6.30	1.70	9.50	4.94	1.92	20.10	7.33	2.74
466	0.27	0.13	64.51	11.10	5.81	36.88	7.86	4.69	101.03	12.99	7.78
485	0.45	0.15	61.74	12.47	4.95	23.23	7.53	3.08	84.81	14.05	6.04
496	0.00	–	36.09	−1.00	–	22.48	−1.00	–	34.45	13.44	2.56
522	−0.40	0.04	193.40	17.51	11.05	451.14	23.72	19.02	642.92	28.82	22.31
535	−0.12	0.06	232.76	20.51	11.35	296.76	19.89	14.92	528.50	27.85	18.98
539	0.53^{l}	–	40.01	9.64	4.15	12.20	−1.00	–	42.86	10.21	4.20
546	0.29	0.03	796.39	33.20	23.99	438.59	23.37	18.77	1231.02	39.92	30.84
556	0.40	0.03	852.52	39.38	21.65	364.81	24.33	14.99	1216.20	45.72	26.60
574	0.38	0.25	25.49	9.11	2.80	11.49	5.44	2.11	36.89	10.03	3.68
578	0.00	–	25.53	−1.00	–	17.39	−1.00	–	23.99	9.57	2.51
583	−0.51	0.06	106.38	14.82	7.18	328.38	20.50	16.02	434.10	24.60	17.65
589	0.17^{u}	–	21.65	−1.00	–	15.29	6.38	2.40	25.84	−1.00	–
591	0.29^{u}	–	50.67	−1.00	–	27.80	10.44	2.66	62.46	18.37	3.40
620	−0.02	0.06	273.77	25.37	10.79	283.93	20.85	13.62	556.98	32.07	17.37
624	0.33^{l}	–	37.22	11.78	3.16	18.61	−1.00	–	45.69	13.11	3.49
625	0.71	0.10	122.38	16.57	7.39	20.79	7.99	2.60	143.04	18.01	7.94
630	0.36^{u}	–	30.65	−1.00	–	14.45	7.37	1.96	34.39	−1.00	–
651	0.40	0.10	146.49	20.77	7.05	62.35	12.44	5.01	208.60	23.66	8.82

Table A5. Flux densities for our 58 sample sources, part 1/2. All values are given in μJy. For sources that are marked with an asterisk, we included the *Spitzer* 3.6 and 4.5 μm flux values in our photometric redshift analysis. The values given for the 3.6 and 4.5 micron channels correspond to the 1 arcsec aperture radius flux values given in the Damen et al. (2011) *Spitzer* catalogue. For the remaining sources, the *Spitzer* values could not be included due to source confusion. We performed our own aperture photometry for the GOODS/ACS (B, V, i, z) and CANDELS (Y, J, H) filters. If an object is not detected in an image (flux < detection threshold), we set $F_\nu = 0$ and $Ferr_\nu$ to the sensitivity limit of the corresponding filter. If an object's position is not covered by the Y band or we are not using the *Spitzer* IRAC data, we mark this with a dash.

	ID	F_ν (B)	$Ferr_\nu$ (B)	F_ν (V)	$Ferr_\nu$ (V)	F_ν (i)	$Ferr_\nu$ (i)	F_ν (z)	$Ferr_\nu$ (z)
*	121	$0.000 \times 10^{+00}$	1.456×10^{-01}	1.023×10^{-01}	1.020×10^{-02}	3.608×10^{-01}	1.631×10^{-02}	$1.142 \times 10^{+00}$	2.010×10^{-02}
*	150	3.147×10^{-02}	1.018×10^{-02}	1.158×10^{-01}	9.915×10^{-03}	1.457×10^{-01}	1.644×10^{-02}	1.670×10^{-01}	1.961×10^{-02}
	173	1.732×10^{-02}	5.131×10^{-03}	8.063×10^{-02}	4.995×10^{-03}	3.987×10^{-01}	8.699×10^{-03}	8.616×10^{-01}	1.063×10^{-02}
*	184	2.607×10^{-02}	8.239×10^{-03}	1.699×10^{-01}	7.821×10^{-03}	6.041×10^{-01}	1.280×10^{-02}	$1.428 \times 10^{+00}$	1.567×10^{-02}
*	189	$0.000 \times 10^{+00}$	3.639×10^{-02}	2.394×10^{-02}	5.045×10^{-03}	4.371×10^{-02}	8.006×10^{-03}	4.974×10^{-02}	9.624×10^{-03}
*	199	$0.000 \times 10^{+00}$	1.456×10^{-01}	5.441×10^{-02}	9.849×10^{-03}	8.621×10^{-02}	1.622×10^{-02}	1.212×10^{-01}	1.954×10^{-02}
	211	2.494×10^{-02}	5.362×10^{-03}	4.317×10^{-02}	4.842×10^{-03}	1.506×10^{-01}	8.124×10^{-03}	3.438×10^{-01}	9.779×10^{-03}
*	217	$0.000 \times 10^{+00}$	8.188×10^{-02}	$0.000 \times 10^{+00}$	7.347×10^{-02}	$0.000 \times 10^{+00}$	1.458×10^{-01}	$0.000 \times 10^{+00}$	2.626×10^{-01}
	221	$0.000 \times 10^{+00}$	8.188×10^{-02}	1.152×10^{-01}	7.800×10^{-03}	1.991×10^{-01}	1.271×10^{-02}	5.681×10^{-01}	1.592×10^{-02}
	226	$0.000 \times 10^{+00}$	1.456×10^{-01}	$0.000 \times 10^{+00}$	1.306×10^{-01}	2.360×10^{-01}	1.371×10^{-02}	8.728×10^{-01}	1.788×10^{-02}
*	242	1.757×10^{-02}	7.810×10^{-03}	9.874×10^{-02}	7.677×10^{-03}	2.477×10^{-01}	1.257×10^{-02}	4.847×10^{-01}	1.555×10^{-02}
*	244	$0.000 \times 10^{+00}$	1.456×10^{-01}	$0.000 \times 10^{+00}$	1.306×10^{-01}	2.279×10^{-02}	1.682×10^{-02}	1.435×10^{-01}	2.036×10^{-02}
	258	$0.000 \times 10^{+00}$	1.310×10^{-02}	$0.000 \times 10^{+00}$	1.176×10^{-02}	1.349×10^{-02}	5.006×10^{-03}	2.765×10^{-02}	6.348×10^{-03}
*	273	$0.000 \times 10^{+00}$	1.456×10^{-01}	$0.000 \times 10^{+00}$	1.306×10^{-01}	$0.000 \times 10^{+00}$	2.592×10^{-01}	6.494×10^{-02}	1.976×10^{-02}
	296	$0.000 \times 10^{+00}$	3.639×10^{-02}	2.533×10^{-02}	4.874×10^{-03}	1.833×10^{-02}	7.507×10^{-03}	1.302×10^{-01}	9.365×10^{-03}
	301	4.095×10^{-02}	1.110×10^{-02}	8.010×10^{-02}	1.080×10^{-02}	9.752×10^{-02}	1.774×10^{-02}	1.430×10^{-01}	2.114×10^{-02}
*	302	$0.000 \times 10^{+00}$	3.639×10^{-02}	4.055×10^{-02}	5.055×10^{-03}	3.643×10^{-02}	8.064×10^{-03}	9.140×10^{-02}	9.936×10^{-03}
	303	$0.000 \times 10^{+00}$	1.456×10^{-01}	2.923×10^{-02}	1.068×10^{-02}	$0.000 \times 10^{+00}$	2.592×10^{-01}	1.952×10^{-01}	2.148×10^{-02}
	306	$0.000 \times 10^{+00}$	8.188×10^{-02}	5.415×10^{-02}	7.566×10^{-03}	7.303×10^{-02}	1.195×10^{-02}	9.642×10^{-02}	1.482×10^{-02}
*	318	$0.000 \times 10^{+00}$	1.456×10^{-01}	8.013×10^{-02}	1.008×10^{-02}	2.476×10^{-01}	1.608×10^{-02}	2.924×10^{-01}	1.966×10^{-02}
*	321	$0.000 \times 10^{+00}$	1.456×10^{-01}	1.114×10^{-01}	9.503×10^{-03}	7.698×10^{-01}	1.630×10^{-02}	$1.699 \times 10^{+00}$	2.023×10^{-02}
	325	7.765×10^{-03}	4.993×10^{-03}	5.990×10^{-02}	5.115×10^{-03}	1.266×10^{-01}	8.440×10^{-03}	2.203×10^{-01}	9.993×10^{-03}
	328	4.020×10^{-02}	9.731×10^{-03}	4.951×10^{-02}	9.514×10^{-03}	1.041×10^{-01}	1.528×10^{-02}	8.870×10^{-02}	1.845×10^{-02}
	331	$0.000 \times 10^{+00}$	3.639×10^{-02}	4.080×10^{-02}	5.182×10^{-03}	9.863×10^{-02}	8.685×10^{-03}	8.005×10^{-02}	1.071×10^{-02}
*	348	$0.000 \times 10^{+00}$	8.188×10^{-02}	1.400×10^{-02}	7.762×10^{-03}	4.749×10^{-02}	1.289×10^{-02}	8.363×10^{-02}	1.612×10^{-02}
*	354	$0.000 \times 10^{+00}$	8.188×10^{-02}	$0.000 \times 10^{+00}$	7.347×10^{-02}	$0.000 \times 10^{+00}$	1.458×10^{-01}	$0.000 \times 10^{+00}$	2.626×10^{-01}
	371	$0.000 \times 10^{+00}$	3.639×10^{-02}	$0.000 \times 10^{+00}$	3.265×10^{-02}	3.466×10^{-02}	7.771×10^{-03}	9.459×10^{-02}	9.689×10^{-03}
	373	3.412×10^{-02}	1.150×10^{-02}	1.111×10^{-01}	1.052×10^{-02}	1.761×10^{-01}	1.624×10^{-02}	1.300×10^{-01}	1.967×10^{-02}
*	389	$0.000 \times 10^{+00}$	3.639×10^{-02}	2.609×10^{-02}	4.989×10^{-03}	7.725×10^{-02}	8.178×10^{-03}	1.560×10^{-01}	9.972×10^{-03}
*	392	$0.000 \times 10^{+00}$	1.456×10^{-01}	$0.000 \times 10^{+00}$	1.306×10^{-01}	$0.000 \times 10^{+00}$	2.592×10^{-01}	$0.000 \times 10^{+00}$	4.669×10^{-01}
*	402	$0.000 \times 10^{+00}$	3.639×10^{-02}	$0.000 \times 10^{+00}$	3.265×10^{-02}	3.582×10^{-02}	9.432×10^{-03}	5.864×10^{-02}	1.138×10^{-02}
	403	8.854×10^{-03}	5.462×10^{-03}	6.888×10^{-02}	5.131×10^{-03}	3.383×10^{-01}	8.065×10^{-03}	3.800×10^{-01}	9.502×10^{-03}
	410	$0.000 \times 10^{+00}$	5.240×10^{-02}	4.042×10^{-02}	5.939×10^{-03}	6.298×10^{-02}	9.611×10^{-03}	1.278×10^{-01}	1.147×10^{-02}
*	428	2.806×10^{-02}	5.212×10^{-03}	4.285×10^{-02}	5.167×10^{-03}	1.195×10^{-01}	8.592×10^{-03}	2.700×10^{-01}	1.009×10^{-02}
	430	$0.000 \times 10^{+00}$	8.188×10^{-02}	$0.000 \times 10^{+00}$	7.347×10^{-02}	$0.000 \times 10^{+00}$	1.458×10^{-01}	$0.000 \times 10^{+00}$	2.626×10^{-01}
*	444	6.266×10^{-03}	5.440×10^{-03}	5.713×10^{-02}	5.092×10^{-03}	6.121×10^{-02}	8.572×10^{-03}	7.174×10^{-02}	1.006×10^{-02}
*	455	6.007×10^{-02}	1.079×10^{-02}	1.837×10^{-01}	1.010×10^{-02}	7.563×10^{-01}	1.743×10^{-02}	$1.708 \times 10^{+00}$	2.037×10^{-02}
	456	$0.000 \times 10^{+00}$	3.639×10^{-02}	$0.000 \times 10^{+00}$	3.265×10^{-02}	$0.000 \times 10^{+00}$	6.480×10^{-02}	$0.000 \times 10^{+00}$	1.167×10^{-01}
*	460	$0.000 \times 10^{+00}$	1.456×10^{-01}	$0.000 \times 10^{+00}$	1.306×10^{-01}	$0.000 \times 10^{+00}$	2.592×10^{-01}	$0.000 \times 10^{+00}$	4.669×10^{-01}
*	462	$0.000 \times 10^{+00}$	3.639×10^{-02}	5.188×10^{-02}	5.007×10^{-03}	1.798×10^{-01}	8.758×10^{-03}	3.492×10^{-01}	1.025×10^{-02}
	466	3.907×10^{-02}	7.866×10^{-03}	6.747×10^{-02}	7.686×10^{-03}	7.346×10^{-02}	1.288×10^{-02}	1.150×10^{-01}	1.525×10^{-02}
*	485	$0.000 \times 10^{+00}$	1.456×10^{-01}	4.446×10^{-02}	9.870×10^{-03}	$0.000 \times 10^{+00}$	2.592×10^{-01}	$0.000 \times 10^{+00}$	4.669×10^{-01}
	496	1.456×10^{-02}	5.231×10^{-03}	4.275×10^{-02}	5.050×10^{-03}	6.628×10^{-02}	8.103×10^{-03}	9.636×10^{-02}	9.832×10^{-03}
	522	$0.000 \times 10^{+00}$	3.639×10^{-02}	1.176×10^{-02}	4.918×10^{-03}	4.276×10^{-02}	8.589×10^{-03}	1.447×10^{-01}	1.002×10^{-02}
	535	$0.000 \times 10^{+00}$	3.639×10^{-02}	6.218×10^{-02}	5.222×10^{-03}	8.202×10^{-02}	8.336×10^{-03}	1.057×10^{-01}	9.989×10^{-03}
*	539	$0.000 \times 10^{+00}$	3.639×10^{-02}	3.697×10^{-02}	4.815×10^{-03}	1.318×10^{-01}	8.382×10^{-03}	1.314×10^{-01}	9.711×10^{-03}
	546	$0.000 \times 10^{+00}$	3.639×10^{-02}	2.176×10^{-01}	5.005×10^{-03}	4.621×10^{-01}	9.036×10^{-03}	5.296×10^{-01}	1.018×10^{-02}
	556	3.312×10^{-02}	1.056×10^{-02}	1.411×10^{-01}	1.296×10^{-02}	2.574×10^{-01}	2.087×10^{-02}	2.370×10^{-01}	2.486×10^{-02}
*	574	$0.000 \times 10^{+00}$	8.188×10^{-02}	$0.000 \times 10^{+00}$	7.347×10^{-02}	$0.000 \times 10^{+00}$	1.458×10^{-01}	4.035×10^{-02}	1.533×10^{-02}
	578	$0.000 \times 10^{+00}$	1.456×10^{-01}	$0.000 \times 10^{+00}$	1.306×10^{-01}	$0.000 \times 10^{+00}$	2.592×10^{-01}	$0.000 \times 10^{+00}$	4.669×10^{-01}
	583	$0.000 \times 10^{+00}$	1.310×10^{-02}	$0.000 \times 10^{+00}$	1.176×10^{-02}	$0.000 \times 10^{+00}$	2.333×10^{-02}	$0.000 \times 10^{+00}$	4.202×10^{-02}
	589	$0.000 \times 10^{+00}$	8.188×10^{-02}	3.719×10^{-02}	7.469×10^{-03}	4.779×10^{-02}	1.195×10^{-02}	1.765×10^{-01}	1.483×10^{-02}
*	591	1.435×10^{-02}	5.530×10^{-03}	1.389×10^{-02}	5.148×10^{-03}	7.005×10^{-02}	8.526×10^{-03}	7.277×10^{-02}	1.048×10^{-02}
	620	$0.000 \times 10^{+00}$	1.456×10^{-01}	6.177×10^{-02}	1.171×10^{-02}	1.533×10^{-01}	1.956×10^{-02}	1.470×10^{-01}	2.419×10^{-02}
	624	$0.000 \times 10^{+00}$	3.639×10^{-02}	$0.000 \times 10^{+00}$	3.265×10^{-02}	5.278×10^{-02}	8.291×10^{-03}	1.104×10^{-01}	1.006×10^{-02}
*	625	2.820×10^{-02}	7.451×10^{-03}	8.857×10^{-02}	7.227×10^{-03}	1.983×10^{-01}	1.082×10^{-02}	5.659×10^{-01}	1.499×10^{-02}
*	630	$0.000 \times 10^{+00}$	1.456×10^{-01}	$0.000 \times 10^{+00}$	1.306×10^{-01}	$0.000 \times 10^{+00}$	2.592×10^{-01}	$0.000 \times 10^{+00}$	4.669×10^{-01}
*	651	$0.000 \times 10^{+00}$	1.456×10^{-01}	5.578×10^{-02}	1.046×10^{-02}	$0.000 \times 10^{+00}$	2.592×10^{-01}	$0.000 \times 10^{+00}$	4.669×10^{-01}

Table A6. Flux densities for our 58 sample sources, part 2/2. All values are given in μJy. For sources that are marked with an asterisk, we included the *Spitzer* 3.6 and 4.5 μm flux values in our photometric redshift analysis. The values given for the 3.6 and 4.5 micron channels correspond to the 1.5 arcsec aperture radius flux values given in the Damen et al. (2011) *Spitzer* catalogue. For the remaining sources, the *Spitzer* values could not be included due to source confusion. We performed our own aperture photometry for the GOODS/ACS (*B*, *V*, *i*, *z*) and CANDELS (*Y*, *J*, *H*) filters. If an object is not detected in an image (flux < detection threshold), we set $F_\nu = 0$ and $Ferr_\nu$ to the sensitivity limit of the corresponding filter. If an object's position is not covered by the *Y* band or we are not using the *Spitzer* IRAC data, we mark this with a dash.

	ID	F_ν (*Y*)	$Ferr_\nu$ (*Y*)	F_ν (*J*)	$Ferr_\nu$ (*J*)	F_ν (*H*)	$Ferr_\nu$ (*H*)	F_ν (3.6μm)	$Ferr_\nu$ (3.6μm)	F_ν (4.5μm)	$Ferr_\nu$ (4.5μm)
*	121	–	–	$3.725 \times 10^{+00}$	4.184×10^{-01}	$7.080 \times 10^{+00}$	6.655×10^{-01}	$1.903 \times 10^{+01}$	2.303×10^{-02}	$1.951 \times 10^{+01}$	3.215×10^{-02}
*	150	1.414×10^{-01}	1.011×10^{-01}	1.316×10^{-01}	1.027×10^{-01}	2.110×10^{-01}	1.419×10^{-01}	2.198×10^{-01}	1.864×10^{-02}	2.503×10^{-01}	2.675×10^{-02}
	173	$1.955 \times 10^{+00}$	2.968×10^{-01}	$3.173 \times 10^{+00}$	3.816×10^{-01}	$4.904 \times 10^{+00}$	5.432×10^{-01}	–	–	–	–
*	184	$3.506 \times 10^{+00}$	3.671×10^{-01}	$6.444 \times 10^{+00}$	5.487×10^{-01}	$9.992 \times 10^{+00}$	7.844×10^{-01}	$1.969 \times 10^{+01}$	2.173×10^{-02}	$2.149 \times 10^{+01}$	3.043×10^{-02}
*	189	2.460×10^{-01}	1.037×10^{-01}	4.377×10^{-01}	1.505×10^{-01}	6.700×10^{-01}	2.119×10^{-01}	$2.374 \times 10^{+00}$	1.810×10^{-02}	$2.794 \times 10^{+00}$	2.589×10^{-02}
*	199	4.411×10^{-01}	1.415×10^{-01}	$1.023 \times 10^{+00}$	2.168×10^{-01}	$3.623 \times 10^{+00}$	4.670×10^{-01}	$1.101 \times 10^{+01}$	1.636×10^{-02}	$1.251 \times 10^{+01}$	2.382×10^{-02}
	211	7.847×10^{-01}	1.956×10^{-01}	$1.483 \times 10^{+00}$	2.775×10^{-01}	$2.422 \times 10^{+00}$	4.072×10^{-01}	–	–	–	–
*	217	$0.000 \times 10^{+00}$	3.690×10^{-02}	$0.000 \times 10^{+00}$	4.437×10^{-02}	$1.513 \times 10^{+00}$	3.104×10^{-01}	$1.105 \times 10^{+01}$	1.756×10^{-02}	$9.509 \times 10^{+00}$	2.579×10^{-02}
	221	$1.295 \times 10^{+00}$	2.458×10^{-01}	$3.136 \times 10^{+00}$	3.735×10^{-01}	$5.550 \times 10^{+00}$	5.733×10^{-01}	–	–	–	–
	226	$1.617 \times 10^{+00}$	2.685×10^{-01}	$2.470 \times 10^{+00}$	3.400×10^{-01}	$4.885 \times 10^{+00}$	5.431×10^{-01}	–	–	–	–
*	242	9.867×10^{-01}	2.119×10^{-01}	$1.963 \times 10^{+00}$	3.022×10^{-01}	$3.120 \times 10^{+00}$	4.334×10^{-01}	$5.839 \times 10^{+00}$	2.194×10^{-02}	$6.199 \times 10^{+00}$	3.032×10^{-02}
*	244	3.466×10^{-01}	2.151×10^{-01}	7.493×10^{-01}	2.027×10^{-01}	$1.297 \times 10^{+00}$	3.026×10^{-01}	$4.891 \times 10^{+00}$	1.617×10^{-02}	$6.214 \times 10^{+00}$	2.290×10^{-02}
	258	$0.000 \times 10^{+00}$	5.904×10^{-03}	6.340×10^{-02}	6.057×10^{-02}	1.584×10^{-01}	1.061×10^{-01}	–	–	–	–
*	273	1.239×10^{-01}	9.358×10^{-02}	3.637×10^{-01}	1.348×10^{-01}	9.127×10^{-01}	2.382×10^{-01}	$6.730 \times 10^{+00}$	2.202×10^{-02}	$9.516 \times 10^{+00}$	3.018×10^{-02}
	296	2.741×10^{-01}	1.138×10^{-01}	5.309×10^{-01}	1.589×10^{-01}	9.128×10^{-01}	2.402×10^{-01}	–	–	–	–
	301	3.404×10^{-01}	1.313×10^{-01}	5.365×10^{-01}	1.617×10^{-01}	$1.115 \times 10^{+00}$	2.615×10^{-01}	–	–	–	–
*	302	1.478×10^{-01}	8.496×10^{-02}	2.512×10^{-01}	1.111×10^{-01}	6.038×10^{-01}	1.943×10^{-01}	$1.255 \times 10^{+00}$	1.634×10^{-02}	$1.484 \times 10^{+00}$	2.333×10^{-02}
	303	–	–	3.929×10^{-01}	1.307×10^{-01}	6.912×10^{-01}	1.977×10^{-01}	–	–	–	–
	306	5.993×10^{-01}	1.672×10^{-01}	$1.153 \times 10^{+00}$	2.333×10^{-01}	$2.350 \times 10^{+00}$	3.808×10^{-01}	–	–	–	–
*	318	–	–	$1.509 \times 10^{+00}$	3.468×10^{-01}	$2.733 \times 10^{+00}$	6.181×10^{-01}	$7.786 \times 10^{+00}$	2.103×10^{-02}	$8.877 \times 10^{+00}$	2.899×10^{-02}
*	321	$3.081 \times 10^{+00}$	3.662×10^{-01}	$4.613 \times 10^{+00}$	4.736×10^{-01}	$6.795 \times 10^{+00}$	6.491×10^{-01}	$1.877 \times 10^{+01}$	2.169×10^{-02}	$1.597 \times 10^{+01}$	2.999×10^{-02}
	325	4.370×10^{-01}	1.395×10^{-01}	$1.071 \times 10^{+00}$	2.191×10^{-01}	$1.815 \times 10^{+00}$	3.293×10^{-01}	–	–	–	–
	328	1.902×10^{-01}	9.893×10^{-02}	1.482×10^{-01}	9.912×10^{-02}	4.256×10^{-01}	1.799×10^{-01}	–	–	–	–
	331	1.179×10^{-01}	7.724×10^{-02}	1.464×10^{-01}	8.201×10^{-02}	2.191×10^{-01}	1.132×10^{-01}	–	–	–	–
*	348	–	–	3.443×10^{-01}	1.377×10^{-01}	9.196×10^{-01}	2.578×10^{-01}	$6.216 \times 10^{+00}$	2.168×10^{-02}	$8.319 \times 10^{+00}$	3.125×10^{-02}
*	354	9.632×10^{-02}	7.838×10^{-02}	1.485×10^{-01}	9.213×10^{-02}	5.986×10^{-01}	1.910×10^{-01}	$2.273 \times 10^{+00}$	2.086×10^{-02}	$2.676 \times 10^{+00}$	3.151×10^{-02}
	371	9.383×10^{-02}	6.683×10^{-02}	1.141×10^{-01}	8.705×10^{-02}	1.917×10^{-01}	1.234×10^{-01}	–	–	–	–
	373	4.063×10^{-01}	1.654×10^{-01}	6.511×10^{-01}	1.886×10^{-01}	$1.143 \times 10^{+00}$	2.762×10^{-01}	–	–	–	–
*	389	4.020×10^{-01}	1.380×10^{-01}	9.805×10^{-01}	2.127×10^{-01}	$1.732 \times 10^{+00}$	3.308×10^{-01}	$3.481 \times 10^{+00}$	2.054×10^{-02}	$3.804 \times 10^{+00}$	2.885×10^{-02}
*	392	–	–	$0.000 \times 10^{+00}$	7.887×10^{-02}	2.602×10^{-01}	1.267×10^{-01}	$2.264 \times 10^{+00}$	2.079×10^{-02}	$3.737 \times 10^{+00}$	2.948×10^{-02}
*	402	1.789×10^{-01}	9.189×10^{-02}	3.553×10^{-01}	1.352×10^{-01}	6.099×10^{-01}	2.008×10^{-01}	$4.111 \times 10^{+00}$	2.116×10^{-02}	$5.718 \times 10^{+00}$	2.951×10^{-02}
	403	4.827×10^{-01}	1.603×10^{-01}	6.172×10^{-01}	1.771×10^{-01}	9.149×10^{-01}	2.434×10^{-01}	–	–	–	–
	410	2.475×10^{-01}	1.170×10^{-01}	5.759×10^{-01}	1.256×10^{-01}	$1.644 \times 10^{+00}$	2.453×10^{-01}	–	–	–	–
*	428	6.167×10^{-01}	1.653×10^{-01}	$1.311 \times 10^{+00}$	2.508×10^{-01}	$2.139 \times 10^{+00}$	3.710×10^{-01}	$4.847 \times 10^{+00}$	1.642×10^{-02}	$5.129 \times 10^{+00}$	2.409×10^{-02}
	430	9.001×10^{-02}	7.286×10^{-02}	1.240×10^{-01}	8.494×10^{-02}	2.034×10^{-01}	1.143×10^{-01}	–	–	–	–
*	444	1.442×10^{-01}	9.279×10^{-02}	2.583×10^{-01}	1.093×10^{-01}	6.724×10^{-01}	2.041×10^{-01}	$2.279 \times 10^{+00}$	1.648×10^{-02}	$2.707 \times 10^{+00}$	2.408×10^{-02}
*	455	$3.046 \times 10^{+00}$	3.809×10^{-01}	$4.355 \times 10^{+00}$	4.483×10^{-01}	$6.243 \times 10^{+00}$	6.130×10^{-01}	$1.000 \times 10^{+01}$	1.539×10^{-02}	$7.745 \times 10^{+00}$	2.226×10^{-02}
	456	–	–	$0.000 \times 10^{+00}$	1.972×10^{-02}	1.595×10^{-01}	1.042×10^{-01}	–	–	–	–
*	460	$0.000 \times 10^{+00}$	6.560×10^{-02}	4.917×10^{-02}	4.868×10^{-02}	2.276×10^{-01}	1.178×10^{-01}	$1.943 \times 10^{+00}$	2.092×10^{-02}	$3.035 \times 10^{+00}$	3.044×10^{-02}
*	462	8.811×10^{-01}	1.941×10^{-01}	$1.758 \times 10^{+00}$	2.863×10^{-01}	$2.474 \times 10^{+00}$	3.865×10^{-01}	$4.591 \times 10^{+00}$	1.567×10^{-02}	$4.518 \times 10^{+00}$	2.253×10^{-02}
	466	2.273×10^{-01}	1.109×10^{-01}	3.608×10^{-01}	1.244×10^{-01}	8.445×10^{-01}	2.213×10^{-01}	–	–	–	–
*	485	$0.000 \times 10^{+00}$	6.560×10^{-02}	$0.000 \times 10^{+00}$	7.887×10^{-02}	1.480×10^{-01}	9.532×10^{-02}	$1.265 \times 10^{+00}$	2.031×10^{-02}	$2.035 \times 10^{+00}$	3.015×10^{-02}
	496	1.241×10^{-01}	8.545×10^{-02}	1.803×10^{-01}	9.386×10^{-02}	4.076×10^{-01}	1.585×10^{-01}	–	–	–	–
	522	–	–	5.377×10^{-01}	1.595×10^{-01}	$1.110 \times 10^{+00}$	2.593×10^{-01}	–	–	–	–
	535	1.596×10^{-01}	8.098×10^{-02}	2.906×10^{-01}	1.086×10^{-01}	7.578×10^{-01}	1.998×10^{-01}	–	–	–	–
*	539	2.196×10^{-01}	1.058×10^{-01}	3.786×10^{-01}	1.309×10^{-01}	$1.383 \times 10^{+00}$	2.879×10^{-01}	$2.816 \times 10^{+00}$	1.619×10^{-02}	$2.987 \times 10^{+00}$	2.334×10^{-02}
	546	6.803×10^{-01}	1.789×10^{-01}	$1.050 \times 10^{+00}$	2.335×10^{-01}	$2.721 \times 10^{+00}$	4.399×10^{-01}	–	–	–	–
	556	5.658×10^{-01}	1.947×10^{-01}	9.578×10^{-01}	2.224×10^{-01}	$1.932 \times 10^{+00}$	3.544×10^{-01}	–	–	–	–
*	574	$0.000 \times 10^{+00}$	3.690×10^{-02}	1.311×10^{-01}	8.630×10^{-02}	4.916×10^{-01}	1.764×10^{-01}	$2.928 \times 10^{+00}$	1.630×10^{-02}	$3.758 \times 10^{+00}$	2.329×10^{-02}
	578	1.273×10^{-01}	9.351×10^{-02}	2.637×10^{-01}	1.184×10^{-01}	4.914×10^{-01}	1.703×10^{-01}	–	–	–	–
	583	$0.000 \times 10^{+00}$	5.904×10^{-03}	1.143×10^{-01}	8.153×10^{-02}	2.614×10^{-01}	1.420×10^{-01}	–	–	–	–
	589	3.272×10^{-01}	1.224×10^{-01}	6.935×10^{-01}	1.810×10^{-01}	8.212×10^{-01}	2.184×10^{-01}	–	–	–	–
*	591	–	–	3.668×10^{-01}	1.347×10^{-01}	8.844×10^{-01}	2.340×10^{-01}	$1.916 \times 10^{+00}$	2.339×10^{-02}	$1.952 \times 10^{+00}$	3.256×10^{-02}
	620	3.080×10^{-01}	1.459×10^{-01}	6.087×10^{-01}	1.814×10^{-01}	$1.486 \times 10^{+00}$	3.091×10^{-01}	–	–	–	–
	624	3.430×10^{-01}	1.603×10^{-01}	6.085×10^{-01}	1.904×10^{-01}	$1.071 \times 10^{+00}$	2.685×10^{-01}	–	–	–	–
*	625	–	–	$2.954 \times 10^{+00}$	3.335×10^{-01}	$5.380 \times 10^{+00}$	5.413×10^{-01}	$2.198 \times 10^{+01}$	2.106×10^{-02}	$2.566 \times 10^{+01}$	3.072×10^{-02}
*	630	–	–	8.553×10^{-02}	6.361×10^{-02}	2.740×10^{-01}	1.292×10^{-01}	$1.181 \times 10^{+00}$	2.124×10^{-02}	$1.529 \times 10^{+00}$	3.052×10^{-02}
*	651	$0.000 \times 10^{+00}$	6.560×10^{-02}	2.284×10^{-01}	1.311×10^{-01}	4.536×10^{-01}	2.005×10^{-01}	$2.134 \times 10^{+00}$	2.122×10^{-02}	$2.797 \times 10^{+00}$	3.177×10^{-02}

Table A7. Magnitude values for our 58 sample sources, part 1/2. All values are given in AB magnitudes. For sources that are marked with an asterisk, we included the *Spitzer* 3.6 and 4.5 μm flux values in our photometric redshift analysis. The values given for the 3.6 and 4.5 micron channels correspond to the 1.5 arcsec aperture radius flux values given in the Damen et al. (2011) *Spitzer* catalogue. For the remaining sources, the *Spitzer* values could not be included due to source confusion. We performed our own aperture photometry for the GOODS/ACS (B, V, i, z) and CANDELS (Y, J, H) filters. If an object is not detected in an image (flux $<$ detection threshold), we set $m_{\rm AB} = 0$ and $merr_{\rm AB}$ to the sensitivity limit of the corresponding filter. If an object's position is not covered by the Y band or we are not using the *Spitzer* IRAC data, we mark this with a dash.

	ID	$m_{\rm AB}$ (B)	$merr_{\rm AB}$ (B)	$m_{\rm AB}$ (V)	$merr_{\rm AB}$ (V)	$m_{\rm AB}$ (i)	$merr_{\rm AB}$ (i)	$m_{\rm AB}$ (z)	$merr_{\rm AB}$ (z)
*	121	0.000	25.992	26.375	0.108	25.007	0.049	23.756	0.019
*	150	27.655	0.351	26.241	0.093	25.991	0.123	25.843	0.127
	173	28.304	0.322	26.634	0.067	24.898	0.024	24.062	0.013
*	184	27.860	0.343	25.825	0.050	24.447	0.023	23.513	0.012
*	189	0.000	27.498	27.952	0.229	27.299	0.199	27.158	0.210
*	199	0.000	25.992	27.061	0.197	26.561	0.204	26.191	0.175
	211	27.908	0.233	27.312	0.122	25.955	0.059	25.059	0.031
*	217	0.000	26.617	0.000	26.735	0.000	25.991	0.000	25.352
	221	0.000	26.617	26.246	0.074	25.652	0.069	24.514	0.030
	226	0.000	25.992	0.000	26.110	25.468	0.063	24.048	0.022
*	242	28.288	0.483	26.414	0.084	25.415	0.055	24.686	0.035
*	244	0.000	25.992	0.000	26.110	28.006	0.801	26.008	0.154
	258	0.000	28.607	0.000	28.724	28.575	0.403	27.796	0.249
*	273	0.000	25.992	0.000	26.110	0.000	25.366	26.869	0.330
	296	0.000	27.498	27.891	0.209	28.242	0.445	26.113	0.078
	301	27.369	0.294	26.641	0.146	26.427	0.198	26.012	0.161
*	302	0.000	27.498	27.380	0.135	27.496	0.240	26.498	0.118
	303	0.000	25.992	27.735	0.397	0.000	25.366	25.674	0.119
	306	0.000	26.617	27.066	0.152	26.741	0.178	26.440	0.167
*	318	0.000	25.992	26.641	0.137	25.416	0.071	25.235	0.073
*	321	0.000	25.992	26.283	0.093	24.184	0.023	23.325	0.013
	325	29.175	0.698	26.956	0.093	26.144	0.072	25.542	0.049
	328	27.389	0.263	27.163	0.209	26.356	0.159	26.530	0.226
	331	0.000	27.498	27.373	0.138	26.415	0.096	26.642	0.145
*	348	0.000	26.617	28.535	0.602	27.208	0.295	26.594	0.209
*	354	0.000	26.617	0.000	26.735	0.000	25.991	0.000	25.352
	371	0.000	27.498	0.000	27.615	27.550	0.243	26.460	0.111
	373	27.567	0.366	26.286	0.103	25.786	0.100	26.115	0.164
*	389	0.000	27.498	27.859	0.208	26.680	0.115	25.917	0.069
*	392	0.000	25.992	0.000	26.110	0.000	25.366	0.000	24.727
*	402	0.000	27.498	0.000	27.615	27.515	0.286	26.980	0.211
	403	29.032	0.670	26.805	0.081	25.077	0.026	24.951	0.027
	410	0.000	27.102	27.384	0.160	26.902	0.166	26.134	0.097
*	428	27.780	0.202	27.320	0.131	26.207	0.078	25.322	0.041
	430	0.000	26.617	0.000	26.735	0.000	25.991	0.000	25.352
*	444	29.408	0.943	27.008	0.097	26.933	0.152	26.761	0.152
*	455	26.953	0.195	25.740	0.060	24.203	0.025	23.319	0.013
	456	0.000	27.498	0.000	27.615	0.000	26.871	0.000	26.232
*	460	0.000	25.992	0.000	26.110	0.000	25.366	0.000	24.727
*	462	0.000	27.498	27.113	0.105	25.763	0.053	25.042	0.032
	466	27.420	0.219	26.827	0.124	26.735	0.190	26.248	0.144
*	485	0.000	25.992	27.280	0.241	0.000	25.366	0.000	24.727
	496	28.492	0.390	27.323	0.128	26.847	0.133	26.440	0.111
	522	0.000	27.498	28.724	0.454	27.322	0.218	25.999	0.075
	535	0.000	27.498	26.916	0.091	26.615	0.110	26.340	0.103
*	539	0.000	27.498	27.480	0.141	26.100	0.069	26.104	0.080
	546	0.000	27.498	25.556	0.025	24.738	0.021	24.590	0.021
	556	27.600	0.346	26.026	0.100	25.373	0.088	25.463	0.114
*	574	0.000	26.617	0.000	26.735	0.000	25.991	27.385	0.412
	578	0.000	25.992	0.000	26.110	0.000	25.366	0.000	24.727
	583	0.000	28.607	0.000	28.724	0.000	27.980	0.000	27.341
	589	0.000	26.617	27.474	0.218	27.202	0.271	25.783	0.091
*	591	28.508	0.418	28.543	0.402	26.786	0.132	26.745	0.156
	620	0.000	25.992	26.923	0.206	25.936	0.139	25.982	0.179
	624	0.000	27.498	0.000	27.615	27.094	0.171	26.293	0.099
*	625	27.774	0.287	26.532	0.089	25.657	0.059	24.518	0.029
*	630	0.000	25.992	0.000	26.110	0.000	25.366	0.000	24.727
*	651	0.000	25.992	27.034	0.204	0.000	25.366	0.000	24.727

Table A8. Magnitude values for our 58 sample sources, part 2/2. All values are given in AB magnitudes. For sources that are marked with an asterisk, we included the *Spitzer* 3.6 and 4.5 μm flux values in our photometric redshift analysis. The values given for the 3.6 and 4.5 micron channels correspond to the 1.5 arcsec aperture radius flux values given in the Damen et al. (2011) *Spitzer* catalogue. For the remaining sources, the *Spitzer* values could not be included due to source confusion. We performed our own aperture photometry for the GOODS/ACS (*B*, *V*, *i*, *z*) and CANDELS (*Y*, *J*, *H*) filters. If an object is not detected in an image (flux < detection threshold), we set $m_{\rm AB} = 0$ and $merr_{\rm AB}$ to the sensitivity limit of the corresponding filter. If an object's position is not covered by the *Y* band or we are not using the *Spitzer* IRAC data, we mark this with a dash.

	ID	$m_{\rm AB}$ (*Y*)	$merr_{\rm AB}$ (*Y*)	$m_{\rm AB}$ (*J*)	$merr_{\rm AB}$ (*J*)	$m_{\rm AB}$ (*H*)	$merr_{\rm AB}$ (*H*)	$m_{\rm AB}$ (3.6μm)	$merr_{\rm AB}$ (3.6μm)	$m_{\rm AB}$ (4.5μm)	$merr_{\rm AB}$ (4.5μm)
*	121	–	–	22.472	0.122	21.775	0.102	20.701	0.001	20.674	0.002
*	150	26.024	0.776	26.102	0.847	25.589	0.730	25.545	0.092	25.404	0.116
	173	23.172	0.165	22.646	0.131	22.174	0.120	–	–	–	–
*	184	22.538	0.114	21.877	0.092	21.401	0.085	20.664	0.001	20.569	0.002
*	189	25.423	0.458	24.797	0.373	24.335	0.343	22.961	0.008	22.784	0.010
*	199	24.789	0.348	23.875	0.230	22.502	0.140	21.296	0.002	21.157	0.002
	211	24.163	0.271	23.472	0.203	22.940	0.183	–	–	–	–
*	217	0.000	27.482	0.000	27.282	23.450	0.223	21.292	0.002	21.455	0.003
	221	23.619	0.206	22.659	0.129	22.039	0.112	–	–	–	–
	226	23.378	0.180	22.918	0.149	22.178	0.121	–	–	–	–
*	242	23.915	0.233	23.168	0.167	22.665	0.151	21.984	0.004	21.919	0.005
*	244	25.050	0.674	24.213	0.294	23.618	0.253	22.177	0.004	21.917	0.004
	258	0.000	29.472	26.895	1.037	25.901	0.727	–	–	–	–
*	273	26.167	0.820	24.998	0.402	23.999	0.283	21.830	0.004	21.454	0.003
	296	25.305	0.451	24.587	0.325	23.999	0.286	–	–	–	–
	301	25.070	0.419	24.576	0.327	23.782	0.255	–	–	–	–
*	302	25.976	0.624	25.400	0.480	24.448	0.349	23.653	0.014	23.471	0.017
	303	–	–	24.914	0.361	24.301	0.311	–	–	–	–
	306	24.456	0.303	23.745	0.220	22.972	0.176	–	–	–	–
*	318	–	–	23.453	0.250	22.808	0.246	21.672	0.003	21.529	0.004
*	321	22.678	0.129	22.240	0.111	21.820	0.104	20.716	0.001	20.892	0.002
	325	24.799	0.347	23.826	0.222	23.253	0.197	–	–	–	–
	328	25.702	0.565	25.973	0.726	24.827	0.459	–	–	–	–
	331	26.221	0.711	25.986	0.608	25.548	0.561	–	–	–	–
*	348	–	–	25.058	0.434	23.991	0.304	21.916	0.004	21.600	0.004
*	354	26.441	0.884	25.971	0.674	24.457	0.346	23.009	0.010	22.831	0.013
	371	26.469	0.773	26.257	0.828	25.693	0.699	–	–	–	–
	373	24.878	0.442	24.366	0.314	23.755	0.262	–	–	–	–
*	389	24.889	0.373	23.921	0.236	23.304	0.207	22.546	0.006	22.449	0.008
*	392	–	–	0.000	26.658	25.362	0.529	23.013	0.010	22.469	0.009
*	402	25.768	0.558	25.024	0.413	24.437	0.357	22.365	0.006	22.007	0.006
	403	24.691	0.361	24.424	0.312	23.997	0.289	–	–	–	–
	410	25.416	0.513	24.499	0.237	23.360	0.162	–	–	–	–
*	428	24.425	0.291	23.606	0.208	23.074	0.188	22.186	0.004	22.125	0.005
	430	26.514	0.879	26.166	0.744	25.629	0.610	–	–	–	–
*	444	26.003	0.699	25.370	0.459	24.331	0.330	23.006	0.008	22.819	0.010
*	455	22.691	0.136	22.303	0.112	21.912	0.107	21.400	0.002	21.677	0.003
	456	–	–	0.000	28.163	25.893	0.709	–	–	–	–
*	460	0.000	26.858	27.171	1.075	25.507	0.562	23.179	0.012	22.695	0.011
*	462	24.037	0.239	23.287	0.177	22.917	0.170	22.245	0.004	22.263	0.005
	466	25.509	0.530	25.007	0.374	24.084	0.285	–	–	–	–
*	485	0.000	26.858	0.000	26.658	25.974	0.699	23.645	0.017	23.129	0.016
	496	26.166	0.748	25.760	0.565	24.874	0.422	–	–	–	–
	522	–	–	24.574	0.322	23.787	0.254	–	–	–	–
	535	25.892	0.551	25.242	0.406	24.201	0.286	–	–	–	–
*	539	25.546	0.523	24.955	0.375	23.548	0.226	22.776	0.006	22.712	0.008
	546	24.318	0.286	23.847	0.241	22.813	0.176	–	–	–	–
	556	24.518	0.374	23.947	0.252	23.185	0.199	–	–	–	–
*	574	0.000	27.482	26.106	0.715	24.671	0.390	22.734	0.006	22.463	0.007
	578	26.138	0.798	25.347	0.487	24.671	0.376	–	–	–	–
	583	0.000	29.472	26.255	0.774	25.357	0.590	–	–	–	–
	589	25.113	0.406	24.297	0.283	24.114	0.289	–	–	–	–
*	591	–	–	24.989	0.399	24.033	0.287	23.194	0.013	23.174	0.018
	620	25.179	0.514	24.439	0.324	23.470	0.226	–	–	–	–
	624	25.062	0.507	24.439	0.340	23.826	0.272	–	–	–	–
*	625	–	–	22.724	0.123	22.073	0.109	20.545	0.001	20.377	0.001
*	630	–	–	26.570	0.807	25.306	0.512	23.719	0.020	23.439	0.022
*	651	0.000	26.858	25.503	0.623	24.758	0.480	23.077	0.011	22.783	0.012

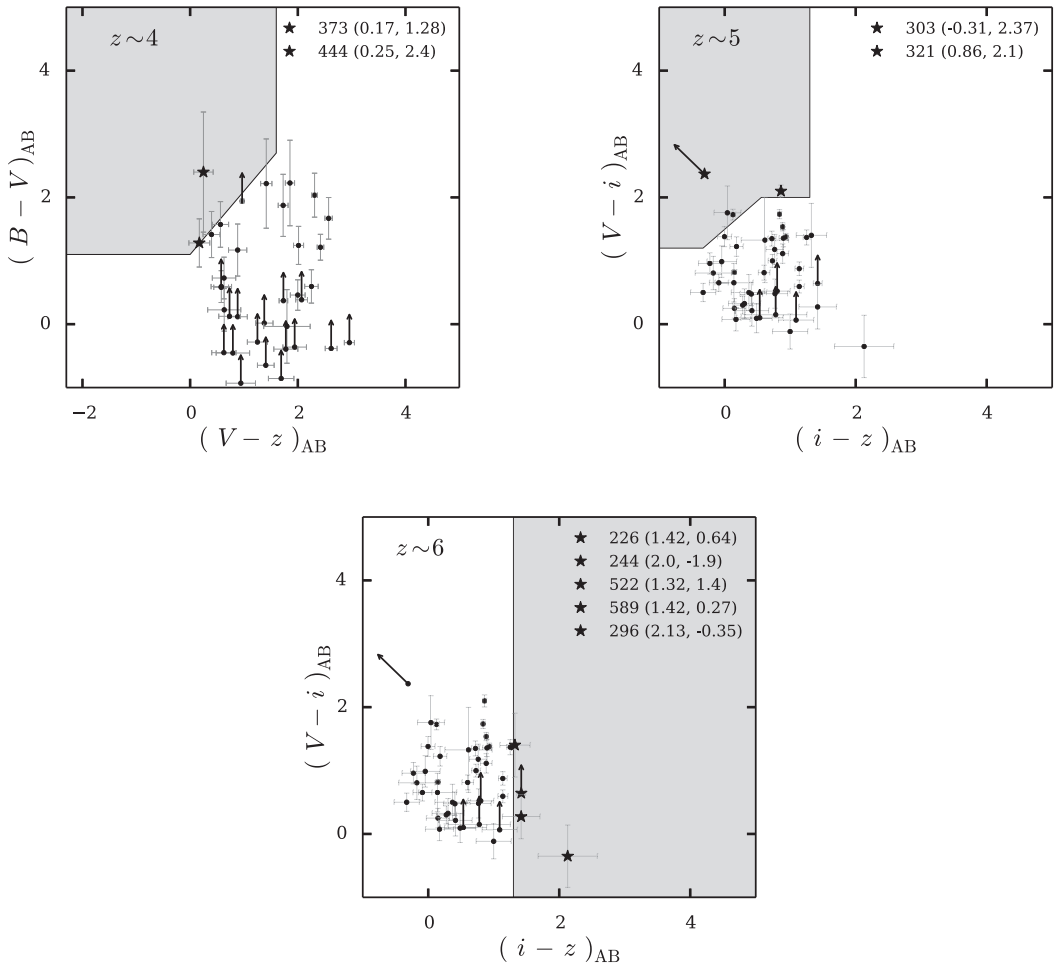

Figure A1. Colour–Colour Diagrams. The sources displayed here were categorized according to the conditions given in Section 3.6. Sources that meet the colour criteria lie in the grey shaded areas and are marked with an asterisk. The upper-left plot illustrates $z \sim 4$ sources. The arrows indicate upper limits in the *B* and in the *z* band. Note that sources with upper limits in the *B* and the V or in the *V* and the *z* filter are not included, since their position cannot be determined. The upper-right panel and the figure at the bottom highlight the position of $z \sim 5$ and $z \sim 6$ sources, respectively.

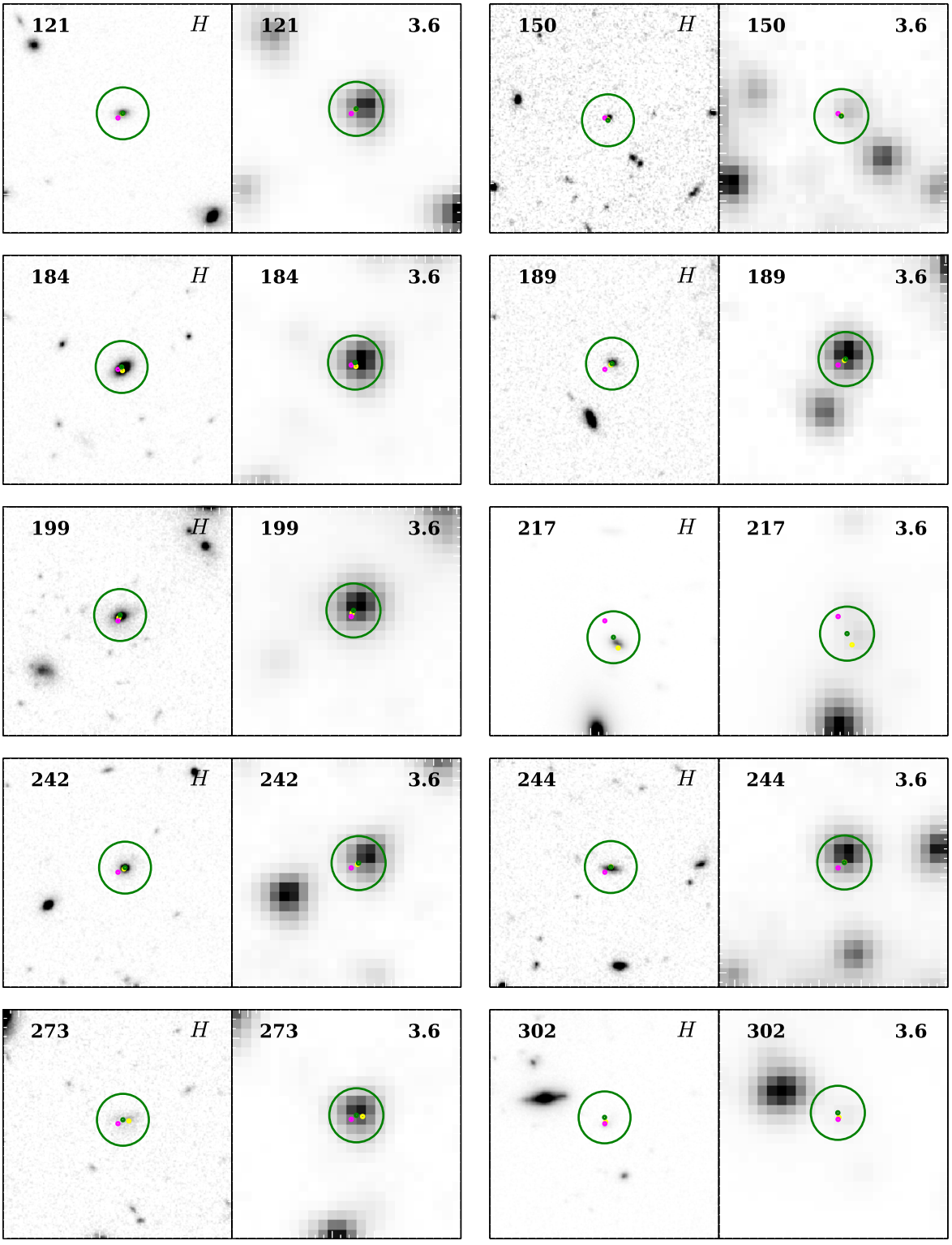

Figure A2. *H* band and 3.6 micron stamps for all objects for which the *Spitzer* flux values are included in the photometric redshift determination, part 1/3. Shown in magenta is the original *Chandra* 4-Ms catalogue position. The yellow circle marks the object's *H*-band position that we determined by running SExtractor. The green point shows the position of the *Spitzer* object closest to the *H*-band position. The green circle around this green point has a radius of 1.7 arcsec. It indicates the PSF size for the 3.6 micron IRAC channel. Due to source confusion the *Spitzer* flux values could not be used for the whole sample. All stamps were colour inverted and are 15 arcsec × 15 arcsec in size.

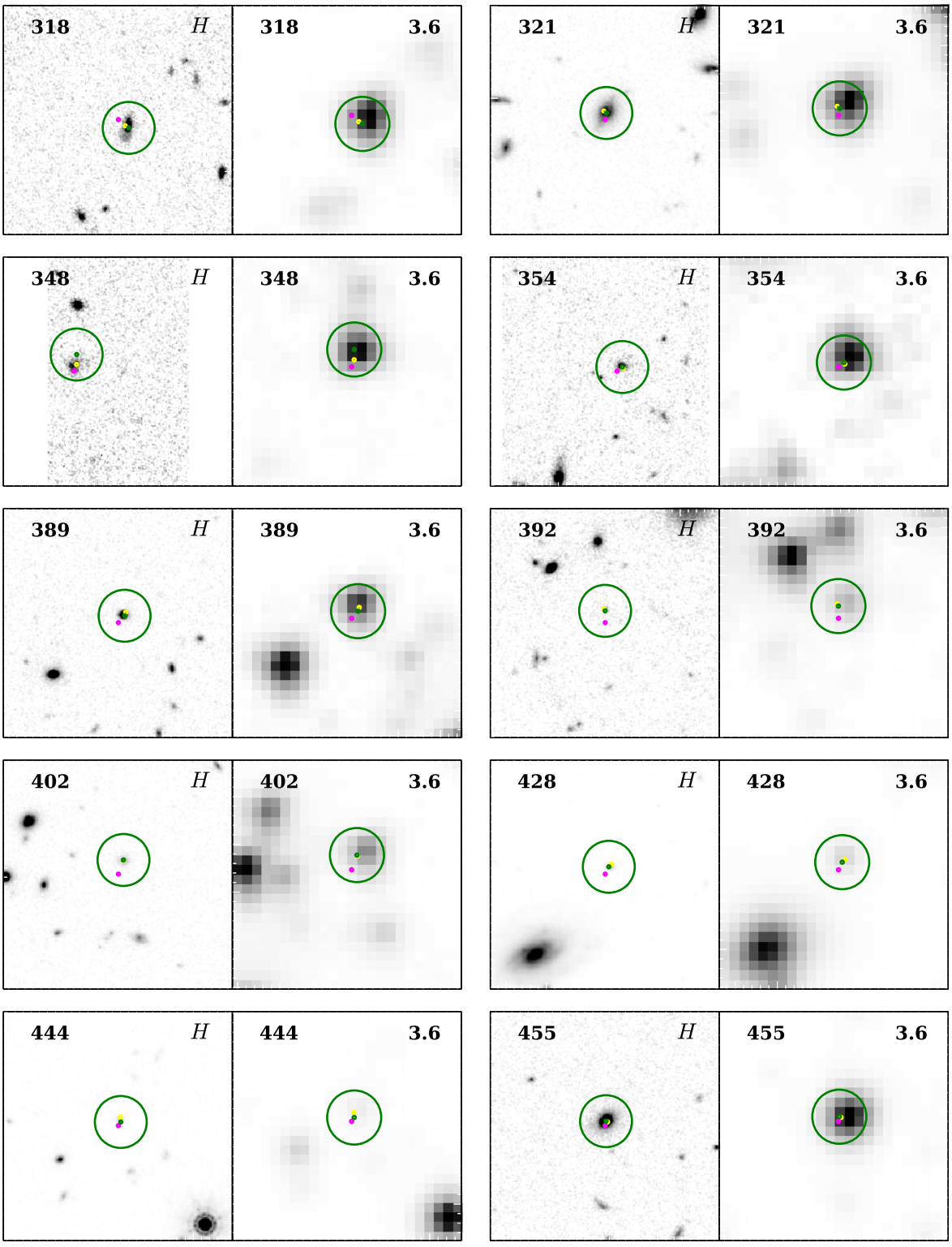

Figure A3. *H* band and 3.6 micron stamps for all objects for which the *Spitzer* flux values are included in the photometric redshift determination, part 2/3. Shown in magenta is the original *Chandra* 4-Ms catalogue position. The yellow circle marks the object's *H*-band position that we determined by running SExtractor. The green point shows the position of the *Spitzer* object closest to the *H*-band position. The green circle around this green point has a radius of 1.7 arcsec. It indicates the PSF size for the 3.6 micron IRAC channel. Due to source confusion the *Spitzer* flux values could not be used for the whole sample. All stamps were colour inverted and are 15 arcsec × 15 arcsec in size.

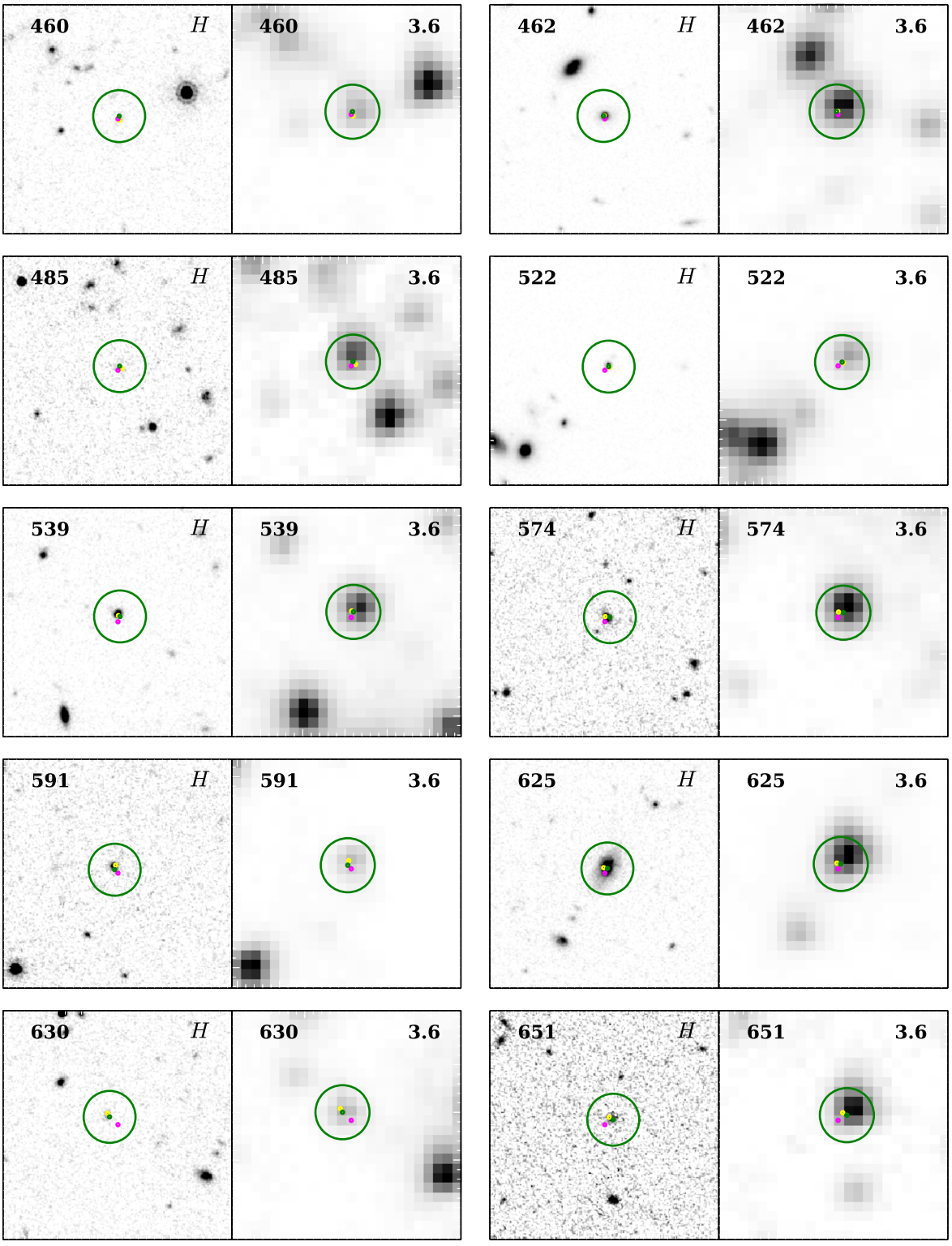

Figure A4. *H* band and 3.6 micron stamps for all objects for which the *Spitzer* flux values are included in the photometric redshift determination, part 3/3. Shown in magenta is the original *Chandra* 4-Ms catalogue position. The yellow circle marks the object's *H*-band position that we determined by running SExtractor. The green point shows the position of the *Spitzer* object closest to the *H*-band position. The green circle around this green point has a radius of 1.7 arcsec. It indicates the PSF size for the 3.6 micron IRAC channel. Due to source confusion the *Spitzer* flux values could not be used for the whole sample. All stamps were colour inverted and are 15 arcsec × 15 arcsec in size.

This paper has been typeset from a TEX/LATEX file prepared by the author.